HRFlexToT: A High Dynamic Range ASIC for Time-of-Flight Positron Emission Tomography

David Sánchez, Sergio Gómez, Joan Mauricio, Lluís Freixas, Andreu Sanuy, Gerard Guixé, Albert López, Rafel Manera, Jesús Marín, Jose M. Pérez, Eduardo Picatoste, Carolina Pujol, Anand Sanmukh, Pedro Rato, Oscar Vela and David Gascón

***Abstract*—Time-of-Flight Positron Emission Tomography (TOF-PET) scanners demand fast and efficient photo-sensors and scintillators coupled to fast readout electronics. This paper presents the HRFlexToT, a 16-channel ASIC for SiPM anode readout manufactured using XFAB 0.18 μm CMOS technology. The main features of the HRFlexToT are a linear Time-over-Threshold (ToT) with an extended dynamic range (10 bits) for energy measurement, low power consumption ($\approx$ 3.5 mW/ch), and an excellent timing response. Experimental measurements show an energy linearity error of $\approx 3\%$ and an energy resolution of about 12% at 511 keV. Single-Photon Time Resolution (SPTR) measurements performed using an FBK SiPM NUV-HD (4 $\times$ 4 mm^2 pixel, 40 μm cell) and a Hamamatsu SiPM S13360-3050CS are around 142 ps and 167 ps full width at half maximum (FWHM), respectively. Coincidence Time Resolution (CTR) measurements with small cross-section pixelated crystals (LSO:Ce,Ca 0.4%, 2 $\times$ 2 $\times$ 5 mm^3) coupled to the same Hamamatsu S13360-3050CS and FBK NUV-HD sensors yield a CTR of 117 ps and 119 ps, respectively. Measurements performed with a large cross-section monolithic crystal (LFS crystal measuring 25 $\times$ 25 $\times$ 20 mm^3) and a Hamamatsu SiPM array S13361-6050NE-04 show a CTR of 324 ps FWHM after time-walk and time-skew correction.**

***Index Terms*—Positron Emission Tomography, TOF-PET, photo-detector technology, SiPM, scintillator, Fast Front-end electronics.**

I. Introduction

PET is a well-established and powerful imaging technique for visualizing and measuring metabolic and biological processes at cellular level [1]–[4]. Improvements to TOF-PET performance reduce the required dose administered to the patient, increase sensitivity, and consequently, lower costs [5], [6]. The main factor affecting TOF-PET imaging performance is system coincidence timing resolution (CTR), which is essentially determined by the combination of scintillator, photo-sensor, and the front-end readout electronics that form the detector in the PET scanner. Improving time resolution leads to better spatial resolution and thus improves the overall PET system [7].

Author S. Gómez works at the Institut d'Estudis Espacials de Catalunya (IEEC), ICCUB (University of Barcelona) (e-mail: sgomez@fqa.ub.edu). Authors D. Sánchez, J. Mauricio, G. Guixé, A. López, R. Manera, D. Gascón, E. Picatoste, C. Pujol, and A. Sanmukh work at the Dept. Física Quàntica i Astrofísica, Institut de Ciències Del Cosmos (ICCUB), University of Barcelona (IEEC-UB), Barcelona, Spain (e-mail: dgascon@fqa.ub.edu, dsanchez@fqa.ub.edu). Authors L. Freixas, J. Marín, J. M. Pérez, P. Rato Mendes, and O. Vela work at CIEMAT, Madrid. David Sánchez and Sergio Gómez are co-first authors.

This study was supported in part by the Industrial PhD program funded by the Catalonian Agency for Management of University and Research Grants, the CLUES project funded by the Spanish MINECO (FPA2016-80917-R), the PET project funded by the Spanish MINECO TEC2015-66002-R and a short-term scientific mission (STSM) funded by COST (European Cooperation in Science and Technology) Action TD1401-FAST.

Manuscript received W, 2020; accepted X. Date of publication Y; date of current version Z.

A. Scintillators, photo-sensors, and fast electronics

Several factors contribute to time resolution, including fluctuations in the gamma-ray depth-of-interaction, the scintillation mechanism itself, and light transport from the point of emission to the sensor [7]. Common scintillator-based gamma-ray detectors for PET employ lutetium oxyorthosilicate (LSO) crystals and lutetium-yttrium oxyorthosilicate (LYSO) doped with cerium because of their good timing resolution, high light yield, and energy resolution [8]. Two types of scintillator arrangements are commonly used in gamma-ray detectors: pixelated crystals [9] and monolithic blocks [10]. Pixelated crystals are formed by a matrix of individual crystals coupled to arrays of photo-sensors (matching the pixel active area or covering part of it), whereas monolithic blocks have a surface covering the active area of several photo-sensors, usually the area of an array of pixels. There are also hybrid scintillator arrangements, such as the long rectangular semi-monolithic option proposed in [11] or the subsurface laser-engraved scintillator crystals described in [12].

Silicon photomultipliers (SiPMs) are one of the most attractive alternatives to photomultiplier tubes (PMTs) in several applications [13], [14], thanks to characteristics such as low operating voltage, small size, compactness, robustness, high-speed response, large intrinsic gain, excellent timing resolution, and immunity to magnetic fields. In contrast, SiPMs show non-linear effects when there is a high number of incident photons, parameter variation (e.g., gain fluctuation) due to over-voltage dependence on temperature and manufacturing process, and noise effects such as optical cross-talk, after-pulsing, and dark count rate, all of which affect the timing response [15]–[17]. Additionally, the photo-detection efficiency (PDE) and single-photon time response (SPTR) of each SiPM are key parameters for obtaining a fast response [7]. Considering all these features, SiPMs represent the most promising photo-sensor devices for TOF-PET applications.

Efficient electronics that are stable and perform at high count rates are also necessary to achieve the best timing performance from photo-sensor devices [4]. In general, such electronics should have the following 6 specifications: Multi-channel SiPM readout; anode voltage adjustment to correct gain differences between channels; low input impedance for a

fast SiPM response; configurable signal shaping to cope with different recovery time constants; low input referred noise; low power consumption. This custom Front-End (FE) electronics should provide a measurement of the arrival time of the gamma photons, an energy measurement, and a trigger signal as main features. All of this information should be digitized using analog- or time-to-digital converters (ADCs or TDCs) [18], [19]. FE electronics and ADCs/TDCs can be implemented in different ASICs (Application Specific Integrated Circuits) or FPGAs (digitization) to minimize any noise from the digital circuitry to the analog FE readout, or in a single ASIC for a more compact design.

B. PET electronics state of the art

Currently, the clinical Siemens Biograph Vision digital PET/CT system has the lowest CTR yet achieved, with a value of ≈210 ps for a complete PET system [20]. In this particular case, the detector block consists of an array of 4 × 4 SiPMs measuring 16 × 16 mm^2 coupled to an array of 5 × 5 LSO pixelated crystals measuring 3.2 × 3.2 × 20 mm^3. The electronics employed in the Vision scanner have not been publically disclosed, but serve as a reference for CTR performance evaluations.

Several ASICs have been developed over the years to provide precise time and energy measurements [21], [22]. For instance, an 8-channel ASIC, referred to as NINO [23], can be employed for time measurements together with some discrete electronics for energy acquisition, as described in [24]. These electronics yield a 64 ps sigma (148 ps FWHM) for single-photon time resolution (SPTR) with a Hamamatsu SiPM S13360-3050CS, and a CTR of 93 ps with 2 × 2 × 5 mm^3 LSO:Ce,Ca crystals and the same SiPM [25]. However, NINO presents the disadvantage of high power consumption (27 mW/ch) and does not provide a linear energy measurement.

An alternative ASIC that provides both time and energy measurements and includes internal TDCs with a time binning of 30 ps is the 32-channel ASIC Petiroc2A [26] developed by Weeroc [27]. This ASIC provides an SPTR of 190 ps FWHM, an energy resolution of 12.9% for 511 keV gamma photon after correction, and a CTR of 223 ps FWHM measured with internal TDCs, using an LSO:Ce,Ca crystal of 3 × 3 × 20 mm^3 and a Hamamatsu SiPM S13360-3050PE. The analog core of the ASIC consumes 6 mW/ch and is capable of processing up to 40k counts/s. The same authors have also proposed the 64-channel TRIROC ASIC, again for PET [28]. This includes a TDC with a 40 ps time bin and consumes 10 mW per channel. Coincidence time resolution measurements employing a LYSO:Ce crystal of 3 × 3 × 10 mm^3 coupled to an ADVANSID NUV SiPM are about 432.7 ps FWHM.

TOFPET2 [21], [22], [29], [30] is an ASIC developed by PETsys Electronics [31] that includes the SiPM readout and internal digitization with TDCs with a time binning of 30 ps. Energy resolution of the 511 keV photopeak is about 8% FWHM and CTR is 202 ps with a LYSO:Ce crystal of 3 × 3 × 5 mm^3 mounted on a KETEK-PM3325-WB SiPM [30]. With 2 × 2 × 3 mm^3 LSO:Ce,Ca crystals and a FBK SiPM NUV-HD (4 × 4 mm^2 pixel, 40 µm cell) or a Hamamatsu SiPM S13361-3050AE-04 [29], the CTR is 118 ps FWHM. Power consumption is about 8.2 mW/ch (depending on the configuration), with digitization and a maximum channel hit rate of 600k counts/s.

A 64-channel ASIC referred as STiC3 (Silicon-Photomultiplier Timing Chip) has also been developed for TOF-PET applications [32], [33]. This ASIC includes a built-in TDC with time binning of 50.2 ps and consumes 25 mW per channel. The STIC3 ASIC is used in combination with the MuTRiG chip to provide a fast digital readout with 1.28 Gbps LVDS serial data links [34]. SPTR measurements performed with a Hamamatsu SiPM S13360-1350CS yielded 150 ps FWHM. A CTR of 214 ps FWHM was obtained using 3.1 × 3.1 × 15 mm^3 LYSO:Ce crystals and a Hamamatsu SiPM S12643-050CN(x), while the energy resolution was ≈12% for 511 keV gamma photons. Moreover, the STIC3 was tested in the SAFIR PET detector using an 8 × 8 array of 2.1 × 2.1 × 12 mm^3 LYSO crystals coupled to a Hamamatsu SiPM S13361-2050AE-08 array, yielding a CTR of 244 ps FWHM [35].

PETA is a 32-channel ASIC family developed for PET [36]. The ASIC has a power consumption of about 40 mW and contains a TDC with time binning of ≈ 50 ps. The PETA3 version achieved a CTR of ≈ 200 ps when using a 3 × 3 × 5 mm^3 LYSO:Ce crystal coupled to a 3 × 3 mm^2 SiPM from FBK, with an energy resolution of ≈12.5% at 511 keV peak.

The FlexToT is a 16-channel ASIC designed for TOF-PET applications [25], [37]–[39]. It achieves an SPTR of 91 ps sigma (214 ps FWHM) and a CTR of 123 ps FWHM with 2 × 2 × 5 mm^3 LSO:Ce,Ca crystals and a Hamamatsu SiPM S13360-3050CS. Power consumption is about 11 mW/ch.

The authors in [40], [41] employ a High Frequency (HF) readout electronics based on two RF amplifiers (BGA616) with a high 3-dB bandwidth of ≈1.5 GHz and a high power consumption of about 360 mW [42]. This large bandwidth electronics serves as a reference to experimentally evaluate the limits of SiPMs and scintillators, or at least to vastly reduce the impact of electronic noise. The HF readout achieves an SPTR of 144 ps FWHM coupled to a Hamamatsu S13360-3050PE SiPM, and a CTR of 75 ps FWHM when using an LSO:Ce Ca 0.4% scintillator measuring 2 × 2 × 3 mm^3. An SPTR of 92 ps FWHM is obtained when employing an FBK SiPM NUV-HD (4 × 4 mm^2 pixel, 40 µm cell), and a CTR of 63 ps FWHM is achieved utilizing the same crystal.

Several of the previously described ASICs include an internal TDC, but digitization can be also performed externally either using a dedicated ASIC [19], [43] or an FPGA-based TDC [44]–[46]. For instance, the MATRIX ASIC includes a 4-channel TDC with 10 ps time resolution and a power consumption of 11 mW/ch [19]. Meanwhile, FPGA-based TDCs are popular due to their lower manufacturing costs and shorter development time, but present higher power consumption and area. Several high-performance FPGA-based TDCs have been reported in recent years with a time resolution of less than 10 ps [45].

The current state of the art as described above will be compared in section V with the electronics presented in this article.

C. Overview

This paper provides an extensive analysis of the 16-channel HRFlexToT (High Resolution Flexible Time-over-Threshold) [47], [48] ASIC, and is organized as follows. The new architecture of the HRFlexToT ASIC is explained in section II, while the experimental setups used are described in section III. Section IV provides a complete performance analysis of the HRFlexToT, including an experimental comparison with the NINO ASIC. The results are discussed in section V and some conclusions are drawn in section VI.

II. Materials: the HRFlexToT ASIC

The HRFlexToT ASIC is designed to provide both time and energy information on the gamma photons detected for each individual input channel. This ASIC is built with a completely redesigned energy measurement readout to provide a linear ToT with an extended dynamic range, while at the same time reducing power consumption and improving the timing response. This enhancement in time resolution yields a better SPTR. Briefly, the HRFlexToT features 16 channels, a high dynamic range, high speed, a low input impedance stage, a common cathode connection, and a directly coupled (DC) input with common-mode voltage control. A block diagram of the HRFlexToT can be seen in Fig. 1.

Information on detected gamma photons is given at each individual output using a CMOS driver with three different possibilities: (1) The time measurement encodes the arrival time of the gamma photons on the rising edge of a pulse with low jitter using a non-linear Time-over-Threshold (ToT) technique; (2) the energy measurement provides a pulse with a linear width with respect to the input current, the so-called Pulse Width Modulation (PWM), employing a linear ToT response; (3) the time plus energy measurement combines the pulse of the timing signal with the pulse of the energy response and thereby encodes the time of arrival and the pulse energy in two consecutive PWM pulses per channel.

Different levels of trigger are also provided in the ASIC: (1) The arrival time measurement is given as a Fast OR between all channels using a low-voltage differential signaling (LVDS) driver and can be also used as a trigger; (2) a low-level trigger pulse with a configurable threshold level set above Dark Count Rate (DCR) noise is provided as an OR between all input channels in CMOS mode; (3) a high-level cluster trigger pulse is obtained as a discriminated sum of a fraction of the input signal from each channel.

A. Input Stage

A low input impedance stage [49] based on a MOSFET current mirror with double feedback loop is employed for SiPM anode readout. Fig. 2 shows the Front-End circuit at transistor level. The Low Frequency feedback loop (LF_{FB}), based on a low input impedance current amplifier with a regulated cascode [50], [51], controls the DC voltage of the input node, thus enabling adjustment of the anode voltage of the SiPM ($\approx$1 V range). This feature can be used to equalize the SiPM response (over-voltage control) and thus compensate non-uniformities in gain or photon detection efficiency of each SiPM. The High Frequency feedback path (HF_{FB}) employs a common-gate regulated cascode configuration [52] to maintain low input impedance at signal bandwidth and thus not affect the fast timing behavior of the SiPM.

The design has been implemented considering that the dominant pole should be set at the input node (SiPM parasitic capacitance is at least in the order of tenths of pF). Using this strategy, stability is not compromised when a sensor with large capacitance is added at the input. The current division scheme at the very front-end part of the circuit splits input current into differently scaled copies which are connected to independent current mirrors to provide the different features of the ASIC, as previously detailed. The main characteristics of the input stage are shown in Table I.

TABLE I
Main characteristics of the HRFlexToT input stage. SPI refers to the Serial Peripheral Interface protocol used to communicate externally with the ASIC.

Feature	Description
Low input impedance	$\approx 35\,\Omega$ along signal bandwidth
Input connection	Anode connection for common cathode arrays
Anode voltage control per channel	1 V (9 bits) dynamic range adjustment with a register configurable via SPI
Bandwidth	Larger than 500 MHz
Input referred noise: - Series noise - Parallel noise	Low for sensor capacitances: 10 pF - 10 nF Lower than 2 nV/$\sqrt{Hz}$ Lower than 20 pA/$\sqrt{Hz}$
Power	Power down mode for each channel

B. Time and Trigger measurement

Time response is achieved by using a leading-edge current comparator, based on [53], just after the input current conveyor, as depicted in Fig. 3. This provides a non-linear Time-over-Threshold (ToT) response encoding the collected charge of the photoelectrons following a pulse width modulation. It also encodes the arrival time of the incoming gamma photons on the rising edge of the generated pulse. The main advantage of this fast comparator is its simplicity, which enables it to provide a fast response with low jitter. In contrast, the main limitation of this kind of ToT comparator is that the relation between the input charge to be measured, i.e., the number of photoelectrons detected, and the width of the encoded pulse is non-linear. Therefore, an alternative readout system is required for the energy measurement. Lastly, the time response is provided as a fast OR between all timing channels using a differential LVDS output, and the individual time response can be read out as a single-ended output per channel.

The ASIC is designed to provide different levels of trigger depending on whether it is used in a single-photon application (e.g., Cherenkov light [41]), for a multi-photon readout where the annihilation photon is captured in a single channel (e.g., scintillation light with a pixelated crystal), or in a multi-photon system with several channels capturing an event (e.g., scintillation light with a monolithic crystal).

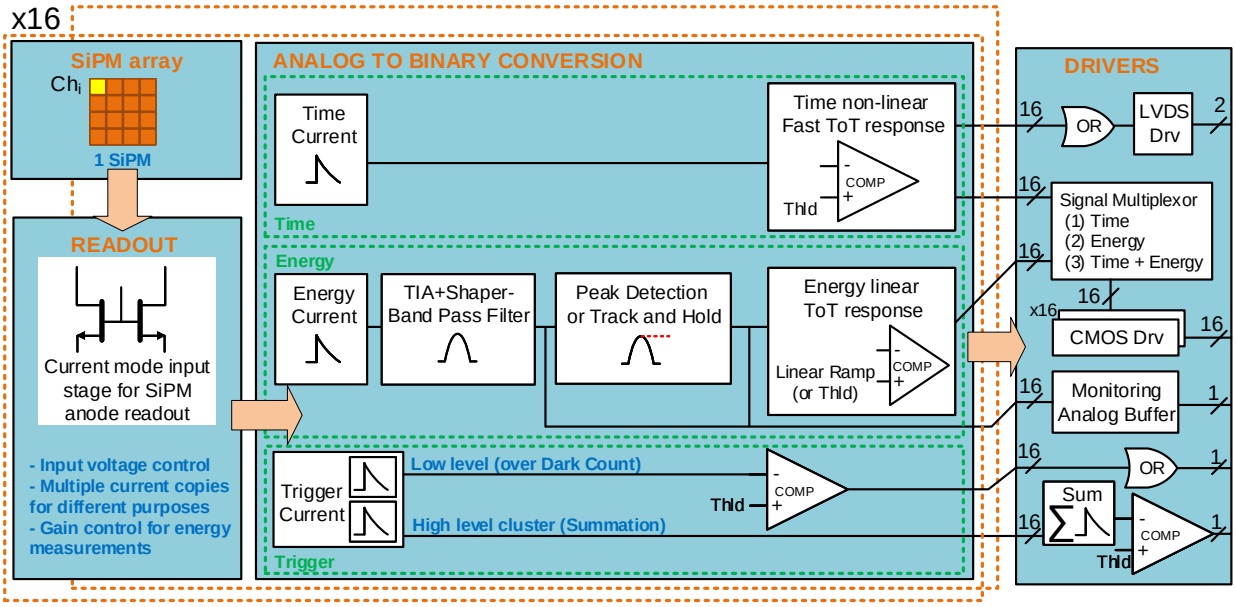

Fig. 1. Functional block diagram of the HRFlexToT ASIC.

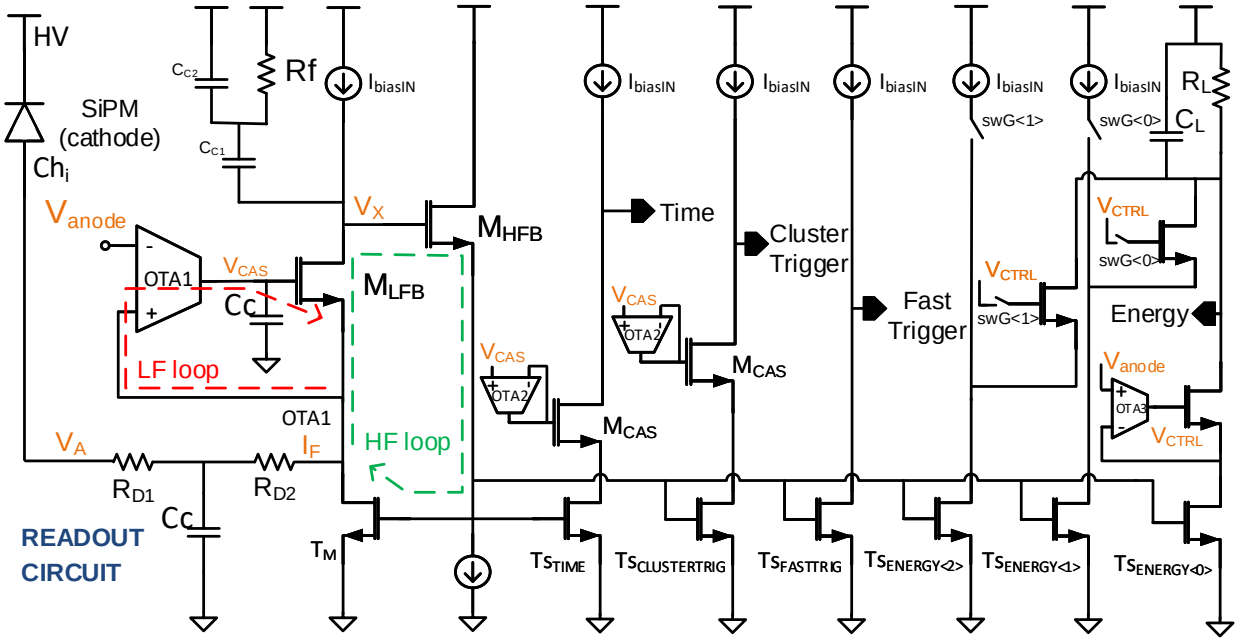

Fig. 2. Input stage Current Conveyor for SiPM readout.

The trigger is provided as a pulse where the rising edge indicates that an event has been detected. A fraction of the input signal is used in a discriminator, the same as that employed for the time signal, to generate a ToT response. This non-linear ToT, referred to as a low-level trigger, is provided as an OR between all channels in CMOS mode. The trigger level is adjustable and must be set above Dark Count Rate (DCR) noise, i.e., a few photoelectrons, to filter out these undesired events. Note that this trigger output is intended for pixelated crystals where the OR between all channels provides information on the first event detected.

A second level of trigger, referred to as high-level cluster trigger, is generated by summing a fraction of the input signal from each channel and then using this as input for the current comparator to generate the discriminated output. This trigger is applicable to monolithic crystals where the signal is spread across several channels and a single channel might not trigger, thus losing the event. Lastly, the time signal can also be used as a trigger in cases where high sensitivity is required and the events are close to the single photoelectron.

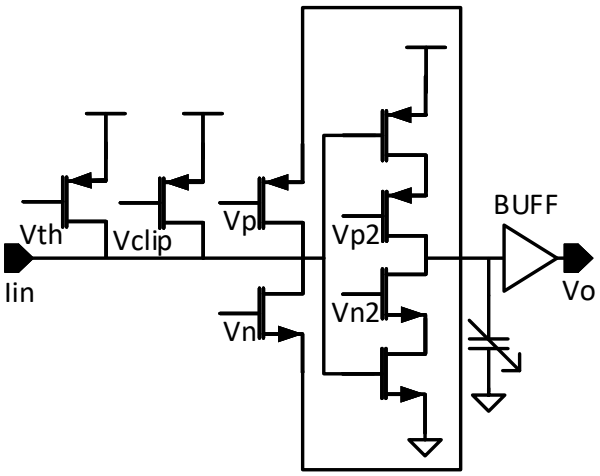

Fig. 3. Leading-Edge current comparator used for Time and Trigger measurements.

C. Energy measurement

The main difference between the HRFlexToT and its predecessor [38] concerns energy processing (Fig. 1). The previous energy measurement circuit consisted of an RC integrator and a constant DC current source. The linear response was achieved by initially charging a capacitor with the incoming signal, then discharging it using a constant DC current, thus providing a linear discharge, and lastly feeding this signal into a voltage discriminator. The problem with this method is that with low currents, discharge of the capacitor stops behaving linearly since part of the DC current starts flowing through the feedback network of the RC integrator instead of discharging the capacitor. This effect with low currents leads to a reduction in the dynamic range (input peak current range is from around 2.5 mA to at least 18 mA) where energy acquisition behaves linearly.

The new energy measurement block, which is conceptually similar to a Wilkinson ADC, does not present this linearity problem with low currents. The redesigned energy path provides a linear ToT output encoding the collected charge in a binary pulse width with an extended dynamic range (input peak current range varies from a few tens of µA up to at least 35 mA). The main improvement in terms of dynamic range is achieved by increasing the minimum current that provides a linear energy response. For instance, with its default configuration the new version can detect pulses with a width of between 0.5 ns (noise floor) and 500 ns, thus yielding a resolution of 10 bits. This increase in sensitivity at low currents is important to preserve the linear response, especially with monolithic crystals where the signal is spread across several channels in SiPM arrays.

Energy acquisition is achieved in three stages, as previously depicted in Fig. 1: (1) a trans-impedance amplifier (TIA) and a Band Pass Filter (BPF) used as a shaper circuit; (2) a Peak Detector and Track and Hold (PDH) circuit and; (3) a ramp generator and a voltage comparator.

The first stage consists of a TIA and a semi-Gaussian shaper, as illustrated in Fig. 4. The energy output from the input stage current conveyor is followed by a closed-loop TIA where the SiPM current signal is converted into voltage for further processing and the output voltage is controlled to maintain linearity. For this purpose, a Miller Operational Transconductance Amplifier (OTA) with a Slew Rate (SR) enhancement circuit based on [54] is employed. The advantage of this SR boosting circuit is that it is only activated when the amplifier detects the incoming event at the input, thus saving on power consumption.

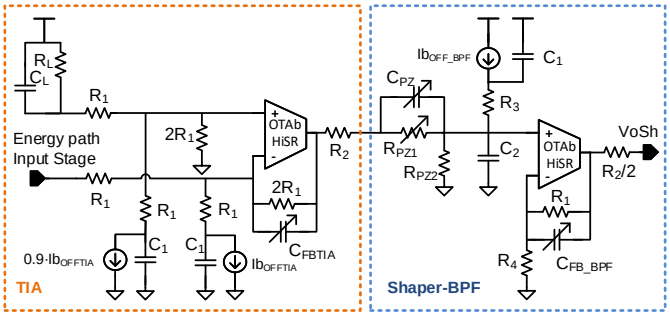

Fig. 4. Energy Measurement: Trans-impedance amplifier and Band Pass Filter (BPF) used as a shaper circuit.

The TIA output is followed by a semi-Gaussian shaper which can be configured to cope with different scintillator and SiPM recovery time constants (up to several hundreds of nanoseconds). The shaper block or Band Pass Filter (BPF) is implemented using a CR-RC pulse shaping network which contains a passive pole-zero cancellation (CR block) and a first-order active integrator (RC block). The purpose of this block is to "shape" the signal by shortening the decay time of the pulse in order to minimize a pile-up of pulses and thus enable a high rate. This effect is achieved by the CR filter. Moreover, the RC filter increases the peaking time of the pulse and thus slew rate requirements are less demanding in subsequent processing stages. More specifically, the CR-RC network can be adjusted by changing the configuration registers via the Serial Peripheral Interface (SPI) bus of the C_{PZ}, R_{PZ1} and C_{FB_BPF} components shown in Fig. 4. Peaking times between 50 to 80 ns can be achieved.

The shaper output is connected to a Peak Detector and Hold (PDH) block, which is implemented based on [55], [56] and detailed in Fig. 5. The PDH circuit operates in two stages. Initially, Write mode (WR) switches are closed and read mode (RD) ones are opened. During this stage, the hold capacitor (C_H) is charged by the input signal (shaper output) until the peak is detected and then holds it, i.e., the circuit tracks the input signal until it reaches its maximum. Then, switches are inverted during the read mode (RD). The PDH is isolated from the input signal to prevent undesired pulses from affecting the detected peak saved in the hold capacitor. In this stage, the amplifier operates as a follower, sending the detected peak (V_{HOLD}) to the next stage in the energy processing chain. The rail-to-rail input/output amplifier with dynamic biasing to minimize power consumption used in [56] is modified, replacing the two-stage amplifier with a classic symmetric OTA [57]. The advantage of this amplifier is that it only has

a low frequency pole and it is easier to stabilize with lower power. Note that the C_c and R_c are used to compensate the Symmetric OTA in the read mode. Once the peak voltage has been processed in the subsequent stage, the (C_H) is discharged and set to the baseline voltage (Vbl) by means of closing the RST switch and thereby enabling the PDH to process the next event.

The original Peak Detector designed by De Geronimo et al. [55], [56], has been modified to include two features. First, a discharge current circuit has been added to eliminate the charge of undesired pulses. The discharge circuit is enabled in the write stage as long as a valid trigger signal is not generated; if an event is detected, the discharge mode is switched off immediately to avoid losing a valid event. Note that this circuit is necessary for the proper behavior of the PDH to avoid saturation caused by the Dark Count Rate (DCR) of the SiPMs. Second, an optional circuit has been added to transform the PDH into a Track and Hold circuit (TH). The TH mode can be employed to capture other moments of the input signal apart from the peak.

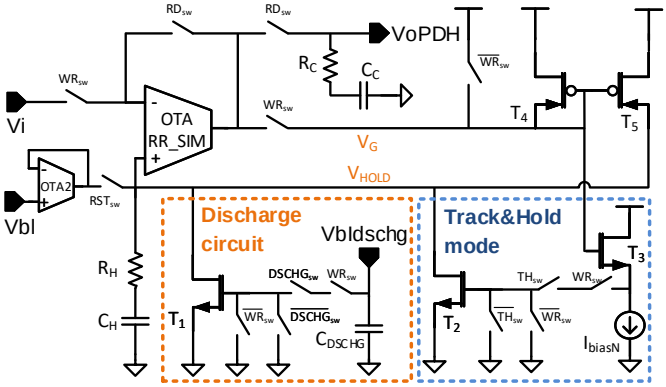

Fig. 5. Energy Measurement: Peak Detector and Track and Hold (PDH) circuit.

Lastly, a rail-to-rail comparator generates a linear ToT energy pulse using the peak detected and a linear ramp signal as a threshold, as illustrated in Fig. 6. Hence, this mechanism provides a linear ToT response since the ramp used as threshold is linear and the amplitude of the incoming signal (encoding the collected charge) follows a linear relation with respect to the number of photoelectrons detected. The ramp is activated once the incoming signal is sampled by the PDH. The ramp generator is based on a DC current source that charges an integrator and is common to all channels. The slope of the ramp is configurable to work with different signal rates. The voltage rail-to-rail comparator consists of a voltage rail-to-rail differential amplifier, a voltage differential amplifier [57], a comparator with internal hysteresis and class AB output stage [58], and a digital buffer. The amplifiers are used to amplify the difference between the input signal and the ramp and thus ease comparison. Lastly, individual control of the threshold at the comparator instead of the ramp is available to provide a non-linear ToT response independent of the ramp.

Energy acquisition is controlled by an asynchronous Finite State Machine (FSM). This control block does not require any

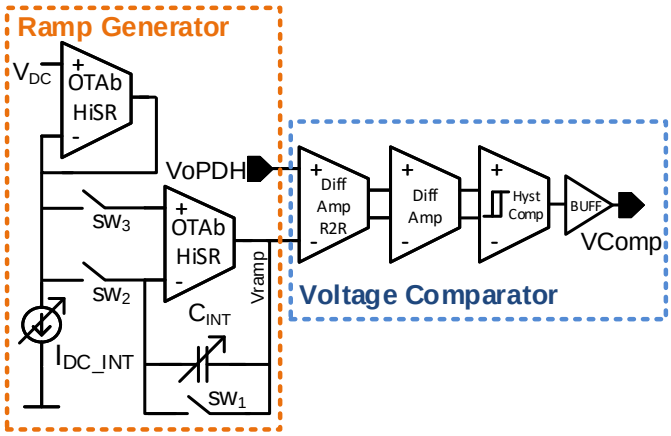

Fig. 6. Energy Measurement: Ramp Generator and voltage comparator.

kind of clock to operate, and thus avoids any simultaneous switching noise produced by digital circuitry. The FSM is illustrated in Fig. 7 and the mechanism to generate the linear energy response is as follows.

1) The system waits until an event is received (detected by any of the triggers) in the *Wait* state.
2) The FSM moves to the *Armed* state waiting for the trigger if time is detected before the trigger. If a trigger signal is not detected within a given period of time, the events are discarded, the FSM returns to the *Wait* state, and the PDH is discharged.
3) The Band Pass Filter shapes the input pulse (*Shaper Start*) and the peak of the shaper output is sampled by the PDH, which is set to Write Mode (WR).
4) When shaping ends (*Shaper Stop*), the system remains in a steady state for a given delay (*Hold*) and the PDH is set to Read Mode (RD).
5) The voltage ramp starts with a DC level below the quiescent voltage of the PDH (*Conversion Start*).
6) The rising edge of the energy pulse is generated once the ramp reaches the first voltage threshold (ThSoC), and then the system moves to the *Conversion* state.
7) A pedestal or minimum energy pulse is generated when the ramp crosses the quiescent level of the PDH. This pedestal can be captured in the absence of a signal and is used for calibration purposes. The pedestal must be subtracted from the energy pulse during data analysis.
8) The falling edge of the energy pulse is generated once the ramp reaches the voltage captured by the PDH.
9) The conversion ends (*Conversion Stop*) when the ramp reaches the second voltage threshold (ThEoC).
10) The system is reset after ending the conversion (*Reset*), and the system returns to the *Wait* state to process the next event.

Fig. 8 shows how the energy pulse is captured and how Time+Energy is multiplexed in the same output as two consecutive pulses. Different triggers can be used for the energy measurement as previously explained in section II-B: the timing signal, the low-level trigger, and the high-level cluster or summation trigger. Moreover, the ASIC provides the

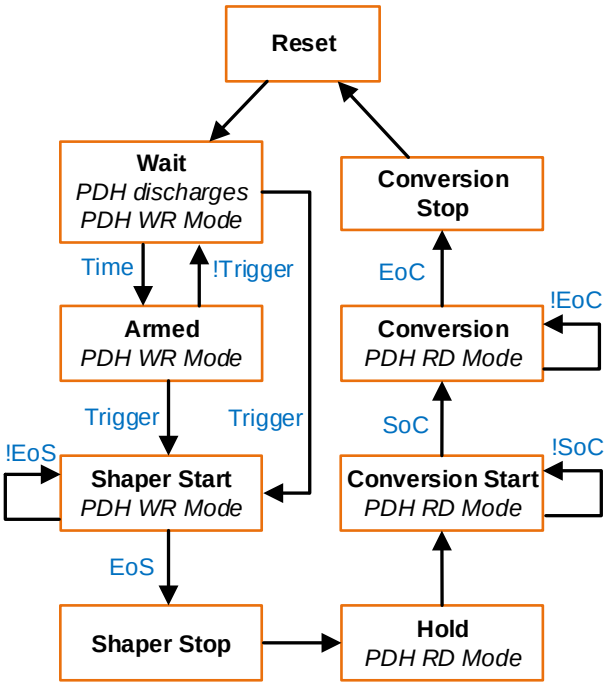

Fig. 7. Finite State Machine used for energy acquisition. EoS, end of shaping; SoC, start of conversion; EoC, end of conversion.

option of including an external trigger for pedestal calibration (minimum pulse width detected in the absence of signal) to compensate for variations between different channels. Lastly, it is important to highlight that the energy processing time can be adjusted, by changing the slope of the ramp, and thus the energy measurement can sustain a trigger rate of around 1M counts/s (1 Mcps).

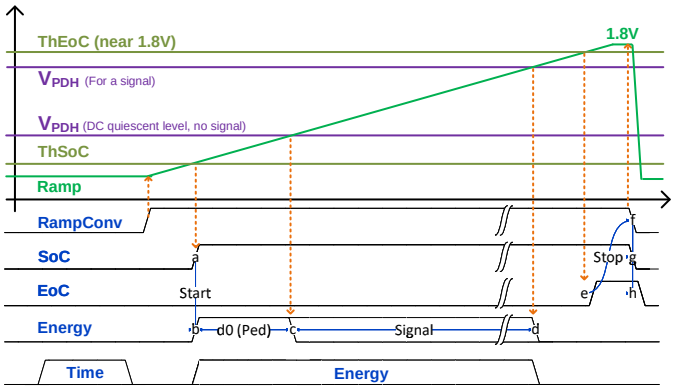

Fig. 8. Energy acquisition mechanism to provide a linear ToT response and example of the Time+Energy output. The time pulse is generated at the time comparator stage and multiplexed into this single output.

III. Methods

This section provides an overview of the experimental setups used to evaluate the performance of the HRFlexToT. A detailed description is given of test bench configuration to show the linearity of the energy measurement, the energy spectroscopy, the SPTR, and the CTR for both pixelated and monolithic crystals.

The DAQ system is based on a Printed circuit board (PCB) basically containing the ASIC, power regulators, connectors, and an Altera Cyclone III FPGA [59], as shown in Fig. 9. The FPGA is used to communicate with the ASIC via SPI in order to change any configuration register in the ASIC. The binary outputs of the HRFlexToT have the form of the output of a fast discriminator, as shown in Fig. 8. They have two levels, which correspond to logical 0 and 1, but as this is not a clocked signal, it is not yet digital and can not be processed by a computer. Digitization must be performed before data analysis using either an ADC or a TDC. In this study, the data are acquired directly via an oscilloscope or are pre-processed with an FPGA-based TDC.

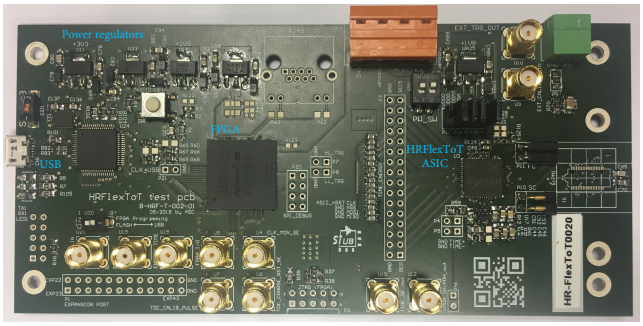

Fig. 9. PCB containing mainly the HRFlexToT ASIC, an Altera Cyclone III FPGA, power regulators, and connectors. The PCB measures 151.05 × 71.43 mm^2.

The FPGA-based TDC IP core consists of 17 channels (1 for the trigger and 16 for individual outputs). This block converts binary input signals to digital by exploiting the FPGA's built-in fast carry sum logic, which is the fastest delay element in the FPGA [44]. The input signal (rising or falling edge) activates the carry propagation in a delay path which is higher than 1 clock period, and thus purposely producing a timing violation. This delay path (64 elements with a typical delay of ≈ 50 ps) is sampled, encoded, buffered, and finally transmitted. In the present case, a speed grade 6 Intel Cyclone III was used, achieving a 40 ps RMS time resolution (94 ps FWHM). Although the design is heavily constrained by the FPGA architecture, this TDC IP core is compatible with Intel Cyclone and MAX families.

A. Linearity of the energy measurement

The linearity test was performed using an electrical pulse injected directly into the HRFlexToT ASIC, as depicted in Fig. 10. An arbitrary waveform generator (Agilent 33250A 80 MHz) that emulates the SiPM signal response sends the pulse to a programmable attenuator (Agilent 11713B). By this means it is possible to sweep a wide range of attenuation factors in order to study the behavior of the ASIC with several signal amplitudes and therefore different input currents (from 30 µA to 35 mA). In this case, the energy measurement was acquired with a Keysight MSOX3094T 350 MHz oscilloscope (5 GS/s).

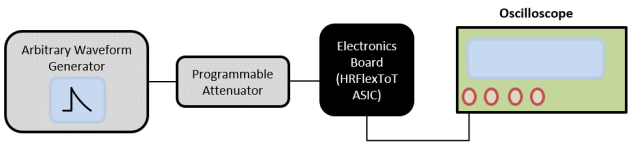

Fig. 10. Schematic representation of the experimental setup used to evaluate the linearity of the energy measurement.

B. Energy spectroscopy

The energy resolution was evaluated using a scintillator crystal wrapped in 3 layers of Teflon and attached to a single channel SiPM. A crystal with a relatively large length was used to maximize capture of the full energy of the arriving gammas, thus recovering the photopeak distribution. The energy measurement provided by the HRFlexToT is encoded in a binary pulse that must be digitized using a TDC. Fig. 11 shows the setup used to obtain the energy spectrum. In this case, the TDC implemented in the FPGA was employed for data acquisition.

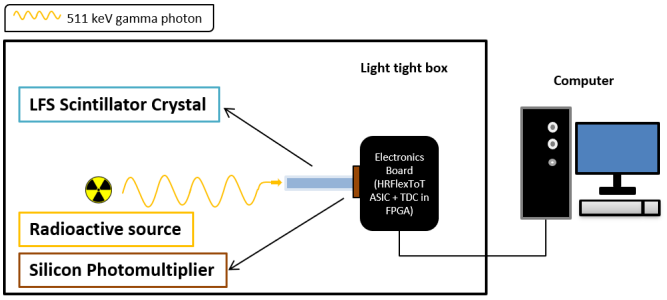

Fig. 11. Schematic representation of the experimental setup to perform spectroscopy.

C. SPTR measurements

The setup used to perform SPTR measurements is shown in Fig. 12. An external trigger at 500 kHz sends a signal to both the laser driver and the oscilloscope. The laser driver sends a pulse to the laser (Picosecond laser diode system 'PiL040X' at 405 nm and a tuned intensity level of 50% as per the optimal operating conditions specified in the user manual, jitter < 3 ps and < 45 ps pulse width from Advanced Laser Diode Systems A.L.S. GmbH). The laser generates a blue photon package that passes through a Single Mode Fiber (Throlabs 305A-FC SM) to a beam collimator. This is coupled to a Thorlabs liquid crystal optical beam attenuator, which can change the attenuation factor depending on the voltage applied (from 0 V to 5 V, minimum to maximum attenuation, respectively). Finally, the beam pulse arrives at a Thorlabs N-BK7 ground glass diffuser, spreading the light homogeneously over the sensor. Additionally, temperature is stabilized at around 15°C to avoid gain variations and reduce dark count noise.

The time per event of each detector is acquired with an Agilent MSO 9404A 4 GHz oscilloscope (20 GS/s). More specifically, this captures the timestamp from the laser trigger, as well as the time signal generated from the photon detected

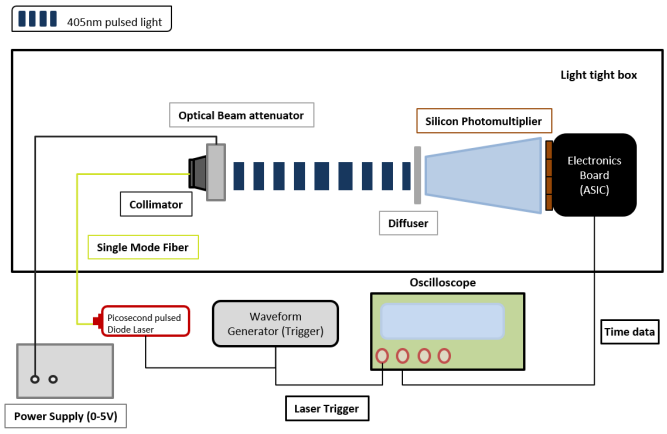

Fig. 12. Schematic representation of the experimental setup using the blue laser source for SPTR measurements. The same setup is used for the red laser source.

by the SiPM and processed by the HRFlexToT leading-edge comparator. The standard deviation of the delay between the trigger and the SiPM signal timestamps, i.e., the jitter corresponding to single cell events, is known as the Single Photon Time Resolution (SPTR). Note that the width of the time signal calculated using the non-linear ToT is required to identify single photon events. Each peak corresponding to the events of the first photon is fitted following the traditional Gaussian approximation method, where the FWHM value of this Gaussian corresponds to the SPTR in FWHM. Moreover, each peak is fitted using a Gaussian convoluted with an exponential approximation, where the FWHM also represents the SPTR and more accurately captures the arrival time of the photons [60].

The SPTR performance of the HRFlexToT was compared to that of its predecessor, FlexToT ASIC [37], [39]. In this study, the same setup as that illustrated in Fig. 12 was utilized, the only difference being that a laser firing red photons was employed (PicoQuant PDL 800-D laser at 635 nm, jitter < 20 ps rms, and 50 ps pulse width). Two consecutive acquisition runs were performed for each ASIC, applying the same over-voltages, system conditions (temperature stable at 18°C in this case), and optimal time threshold.

D. CTR measurements with pixelated scintillators

The CTR obtained using different scintillator crystals and SiPMs was evaluated and compared between the NINO ASIC, the FlexToT version, and the HRFlexToT at CERN Crystal Clear lab. The NINO ASIC readout with some discrete electronics used for CTR measurements is described in [24]. The process starts with the annihilation of the positron emitted by the ^{22}Na radioactive source, generating two gamma photons of 511 keV traveling in a back-to-back configuration. These are captured by two scintillator crystals and converted into optical photons in an optical range typically between 400-600 nm. A fraction of those photons will arrive at the photo-sensor, in this case a SiPM, and generate a current signal that will be collected by the FE electronics to extract both energy and time information. The setup configuration is shown in Fig. 13.

Note that all measurements were taken in an isolated light tight box at a constant temperature of 20°C if no other condition is specified.

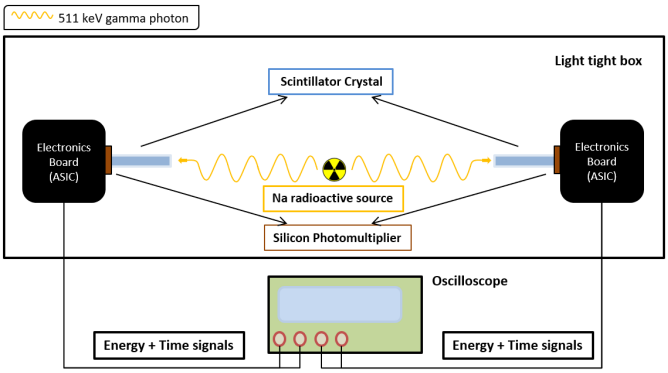

Fig. 13. Schematic representation of the experimental setup for gamma coincidence measurements.

The energy and time per event of each detector was acquired with an Agilent MSO 9404A 4 GHz oscilloscope (20 GS/s). The delay time was calculated as the arrival time difference between the two gamma photons captured in the two electronic boards containing the ASIC under study. Events within 3 sigma from the mean photopeak at 511 keV were used to compute the CTR.

Different crystal lengths were employed in this study, with 5 mm long crystals being used to evaluate the best possible performance of the ASIC. Smaller crystals show less time jitter degradation due to a smaller spread in light transport from the point of emission to the photo-detector [7], although 5 mm long crystals are not commonly used in standard PET because detector efficiency increases with scintillator crystal thickness. Nowadays, 20 mm long crystals are extensively used in PET devices [20] as the best trade-off between cost, efficiency, and performance; small variations such as 18 mm length can be also utilized, as seen in [61]. Consequently, we also evaluated the HRFlexToT ASIC when increasing crystal length up to 20 mm.

E. CTR measurements with monolithic scintillators

In monolithic crystals, the scintillation light is shared among many SiPM channels and the amount of collected photons in each channel is a fraction of the total number of optical photons emitted in a single gamma absorption. Therefore, timing and energy information on the collected events is spread between the different channels of the ASIC.

Measurements with monolithic scintillators were performed using the setup illustrated in Fig. 14, which is similar to the test bench used for pixelated crystals. In this case, one of the detectors employs a monolithic crystal and the other uses a known reference detector. These measurements were performed using a $2 \times 2 \times 5$ mm^3 LSO:Ce Ca 0.4% coupled to a S13360-3050CS as a reference detector with 90 ps FWHM jitter. The time and energy information in each channel was digitized with the TDC implemented in the FPGA with 94 ps FWHM time bin resolution.

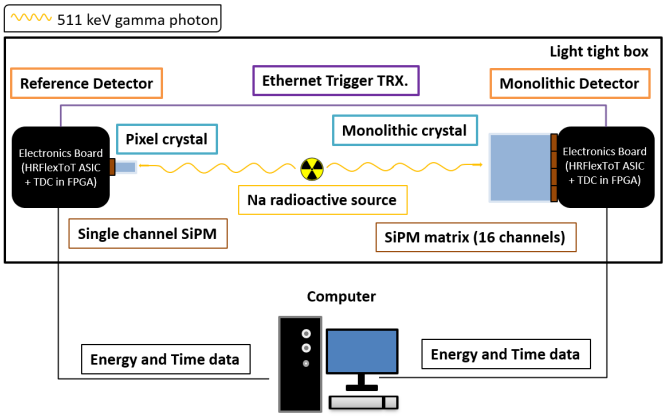

Fig. 14. Schematic representation of the experimental setup for gamma coincidence measurements with a monolithic crystal and a reference detector.

IV. HRFlexToT Performance Evaluation

The new, redesigned HRFlexToT ASIC presents lower power consumption, reduced from 11 mW/ch to 3.5 mW/ch thanks to the use of XFAB 0.18 µm CMOS technology instead of the AMS 0.35 µm HBT BiCMOS technology utilized in the FlexToT. The aim of this section is to illustrate the potential capabilities of the HRFlexToT through various experimental tests to determine: (1) the linearity and resolution of the energy acquisition system; (2) SPTR measurements performed with different SiPMs; (3) CTR performance by means of ASIC tests with pixelated and monolithic crystals.

A. Linearity of the energy measurement

In a real detector system, the number of optical photons collected by the sensor is directly related to the energy deposited by the original gamma ray in the scintillator crystal. A good energy resolution over a wide range of energies is required in several applications to achieve the best detector performance and, thus optimize the quality of the reconstructed image.

The HRFlexToT can be configured with several gain modes that model the dynamic range response. As an example, Fig. 15 shows the highest and lowest gain configurations. The maximum gain should be used for very low light levels (single photon), whereas the minimum gain should be used for events where high numbers of optical photons are collected (gamma-ray detection using segmented scintillator crystals).

The energy response behaves linearly for different gain configurations with a maximum linearity error of approximately $\pm 3\%$. Lastly, this test was performed for all 16 channels, obtaining a gain uniformity error of less than 2% between the different channels for both gain configurations.

B. Energy spectroscopy

The energy resolution was measured using an LFS crystal measuring $3 \times 3 \times 20$ mm^3 attached to a single channel Hamamatsu (HPK) SiPM S13360-3050CS (3 x 3 mm^2 pixel, 50 µm cell). Fig. 16 illustrates a gamma-ray spectroscopy with two radiation sources, ^{22}Na and ^{137}Cs, with activities of 370

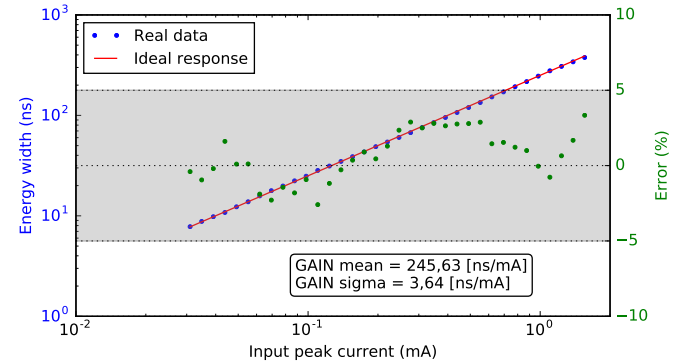

(a) Highest gain configuration.

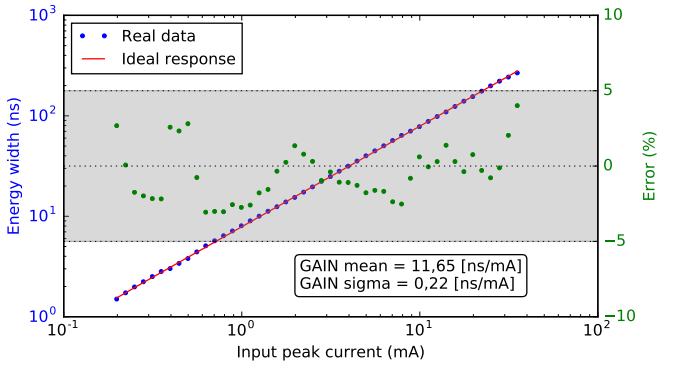

(b) Lowest gain configuration.

Fig. 15. Energy measurement for a given channel (all behave similarly) and the associated error at the lowest gain. Gain mean and sigma between the 16 channels is also shown.

kBq and 100 kBq, respectively, and assuming simultaneous measurement.

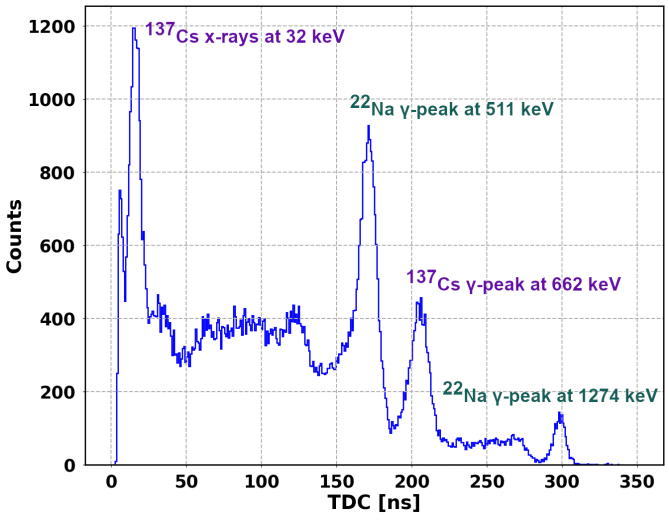

Fig. 16. ^{22}Na and ^{137}Cs spectrum in pulse width units (ns) using the HRFlexToT ASIC and the TDC from the FPGA.

Fig. 16 clearly shows a linearity problem since the distance from 0 to the first ^{22}Na γ-peak at 511 keV is greater than the distance between this peak and the second ^{22}Na γ-peak at 1274 keV. As previously seen, the ASIC configured in a low gain mode has a large dynamic range and thus the energy response should not be saturated. The SiPM S13360-3050CS reaches saturation above 2000 fired micro-cells [17], whereas the expected number of optical photons reaching the scintillator surface might be close to 7000. Hence, saturation effects might be observed, depending on photon collection efficiency (a combination of fill factor and quantum efficiency). Note that the scintillator might also present non-linear responses for large energy deposits, but in this experiment, correcting the SiPM response ensure a linear spectrum. Lastly, besides correcting the linearity of the system, the TDC response must be calibrated into keV for spectroscopy measurements.

The following equation takes into account this saturation effect to linearize the scale of the system [17]:

$$N_{photon} \cdot PDE = -N_{total} \cdot ln\left[1 - \frac{N_{fired}}{N_{total}}\right] \quad (1)$$

where N_{photon} is the number of photons arriving at the sensor, PDE stands for Photon Detection Efficiency, N_{total} is the total number of micro-cells, and N_{fired} is the number of fired micro-cells. Thus, the $N_{photon} \cdot PDE$ captures the detected photons following a linear behavior. In particular, N_{fired} is directly related to the collected energy following the expression:

$$N_{fired} = TDC[ns] \cdot f \quad (2)$$

where $TDC[ns]$ is the width of the energy signal in nanoseconds and f is the calibration factor corresponding to the number of fired micro-cells per nanosecond of the energy pulse width, i.e., the energy gain in photons/nanosecond units. The calibration factor f can be found using the energy ratio of the gamma peaks from the ^{22}Na source and the ratio of the detected photons at those energies as follows.

$$\frac{N_{photon} \cdot PDE[1274keV]}{N_{photon} \cdot PDE[511keV]} = \frac{1274}{511} = 2.49 \quad (3)$$

The linearized energy spectrum could be represented in terms of detected photons ($N_{photon} \cdot PDE$) using the calibration factor f and equation 2. Then, the energy in terms of electron-volts could be obtained using the detected photons as follows:

$$N_{photon} \cdot PDE = a + b * Energy[keV] \quad (4)$$

where a and b are coefficients that can be obtained as the linear regression equation of several calibration points. Fig. 17 shows the linear regression to calibrate the system using the most significant peaks of several radiations sources: ^{22}Na (Compton backscatter peak, Compton Edge, 511 keV and 1274 keV gammas), ^{137}Cs (X-rays at 32 keV and 662 keV gamma peak), ^{241}Am (26 keV and 60 keV gamma peaks) and ^{60}Co (1173 keV and 1333 keV).

Fig. 18 illustrates the linearized energy spectrum in terms of keV for the two radiation sources, ^{22}Na and ^{137}Cs. Note that the gamma photopeaks of both radiation sources can be perfectly identified at their corresponding energy. Lastly,

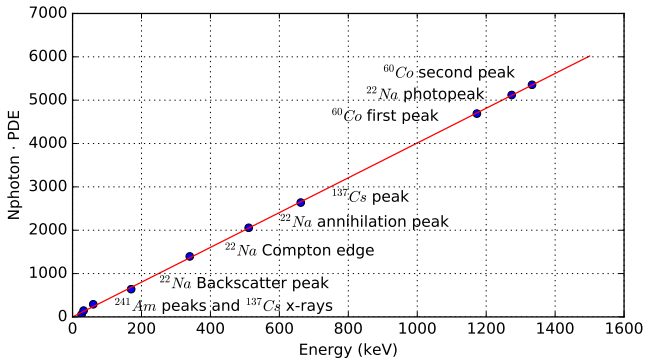

Fig. 17. Linear regression to calibrate the energy system with several radioactive sources.

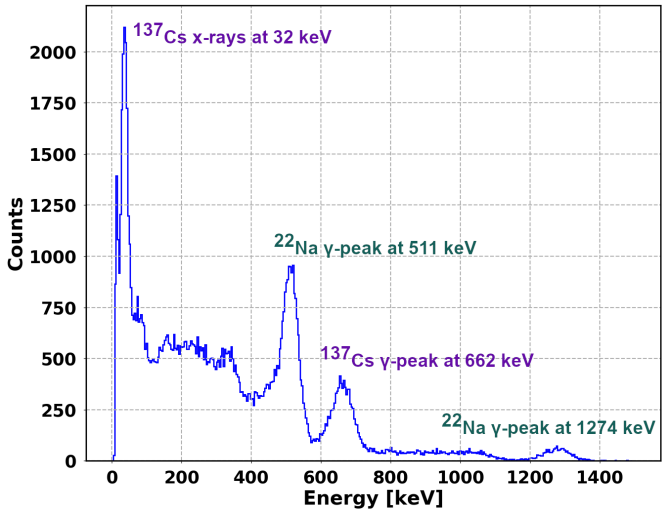

Fig. 18. ^{22}Na and ^{137}Cs spectrum in calibrated energy units (keV) using the HRFlexToT ASIC and the TDC from the FPGA after linearization of the SiPM response.

the energy resolution of a given radiation source, R, can be obtained using the following expression:

$$R = \frac{FWHM}{\mu} \tag{5}$$

where $FWHM$ is the full width at half maximum and μ is the mean of the Gaussian fit for a specific detected peak. The resolution at 511 keV from ^{22}Na is 12.06% and the resolution at 662 keV from ^{137}Cs is 10.19%.

C. SPTR measurements

SPTR measurements can be seen in Fig. 19 and Fig. 20 for the Hamamatsu SiPM S13360-3050CS and the Fondazione Bruno Kessler (FBK) SiPM NUV-HD (4 × 4 mm^2 pixel, 40 µm cell), respectively. These figures illustrate the different photons captured (or firing cells) in the top plot, and the corresponding SPTR distribution in the bottom one. A time jitter of 142 ps FWHM was found when using this configuration with the FBK SiPM NUV-HD and of 167 ps FWHM with the Hamamatsu SiPM S13360-3050CS, both with the HRFlexToT ASIC. Additionally, Table II gives a comparison of the HRFlexToT and the NINO ASIC [23], [25], [40] in terms of SPTR, showing that both ASICs achieve an excellent timing performance.

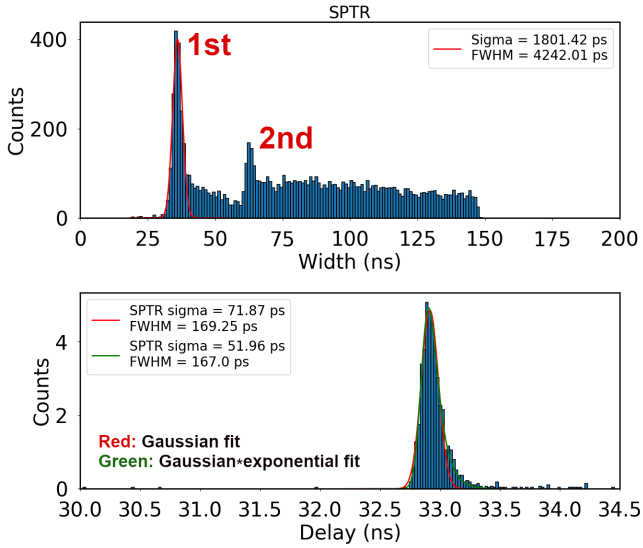

Fig. 19. (Above) non-linear ToT width distribution and (below) delay of arrival time of the first photon using HPK SiPM S13360-3050CS (3 × 3 mm^2 pixel, 50 µm cell).

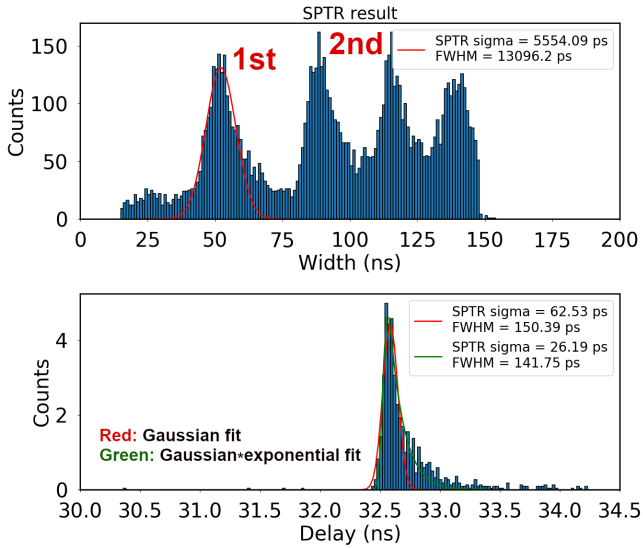

Fig. 20. (Above) non-linear ToT width distribution and (below) delay of arrival time of the first photon using FBK SiPM NUV-HD (4 × 4 mm^2 pixel, 40 µm cell).

The SPTR performance of the HRFlexToT was also compared to that of its predecessor, the FlexToT ASIC. Fig. 21 shows the SPTR comparison between both ASICs. As can be seen, an improvement of around 30-40% was obtained in the time resolution depending on the over-voltage, with 3 times less power consumption. Note that the minimum SPTR (60 ps) achieved in this experiment was lower compared to the SPTR

TABLE II
SPTR COMPARISON IN FWHM BETWEEN THE HRFLEXTOT AND NINO ASIC FOR THE BEST OVER-VOLTAGE (VoV).

SiPM	NINO	HRFlexToT
HPK S13360-3050CS (3×3 mm^2 pixel, 50 µm cell)	160 ps FWHM (10 V of VoV)	167 ps FWHM (10 V of VoV)
FBK NUV-HD (4×4 mm^2 pixel, 40 µm cell)	135 ps FWHM (12 V of VoV)	142 ps FWHM (11.5 V of VoV)

(71 ps) shown in Fig. 19 for the same HPK SiPM S13360-3050CS.

One possible reason for this difference in SPTR may be the internal structure of the HPK SiPM S13360-3050CS model, which is built on a p-on-n buried junction structure [62]. Red photons are mainly but not exclusively absorbed beneath the junction where holes can trigger the avalanche, whereas photogeneration of blue photons only occurs close to the surface above the junction, where only electrons trigger the avalanche. Note that red photons penetrate deeper into the surface because the photon absorption length of silicon increases with wavelength [63]. This difference in the absorption point results in more penetration time spread toward the buried junction for blue photons and thus slightly greater jitter [64]. Note that this p-on-n structure is considered blue sensitive, despite having better SPTR for red photons, since holes have a lower triggering probability than electrons and thus lower PDE for red wavelengths and higher PDE in the blue spectrum [14] (PDE at 405 nm is ≈36% whereas PDE at 635 nm is ≈24% when considering 3 V of over-voltage [65]). Hence, this sensor is perfectly suitable for CTR measurements in a PET module where most of the events are captured in the blue region.

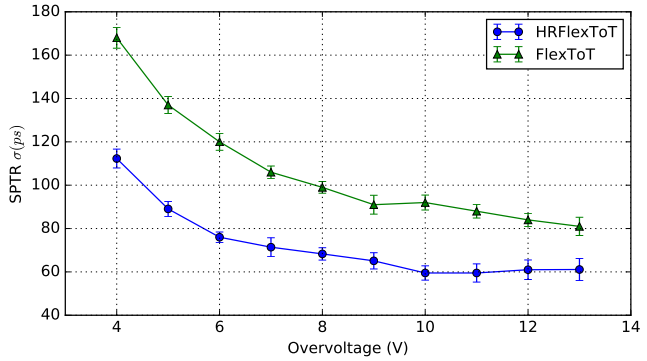

Fig. 21. SPTR comparison between the new HRFlexToT and the FlexToT. Sensor used: HPK SiPM S13360-3050CS (3×3 mm^2 pixel, 50 µm cell).

D. CTR measurements with pixelated scintillators

This section provides different CTR measurements employing the HRFlexToT, the NINO ASIC, and the FlexToT version. An example of the figure of merit for a typical CTR measurement can be seen in Fig. 22. In this configuration, a small LSO:Ce Ca 0.4% co-doped scintillator crystal measuring $2 \times 2 \times 5$ mm^3 is attached to the 3×3 mm^2 Hamamatsu SiPM S13360-3050CS. The plots at the top correspond to the energy deposited on each detector, where the 511 keV photopeak can be identified in the highlighted region at around 300 ns of the energy pulse width. Note that the second peak from the typical ^{22}Na spectrum is not visible because the trigger is set to coincidence mode, and only events where both 511 keV gammas deposit energy on the crystal are recorded. The delay time between detectors for the events corresponding to the 511 keV peak is shown in the bottom plot. A CTR of 117 ps FWHM was achieved with the Hamamatsu SiPM S13360-3050CS.

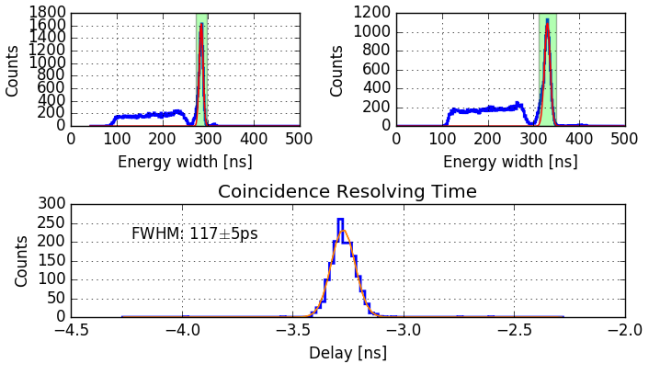

Fig. 22. CTR measurement with LSO:Ce Ca 0.4% measuring $2 \times 2 \times 5$ mm^3 coupled to a S13360-3050CS SiPM at 8 V of over-voltage.

The same crystal pair was used to measure the CTR when coupled with an FBK SiPM NUV-HD (4×4 mm^2 pixel, 40 µm cell), as can be seen in Fig. 23. The HRFlexToT readout shows that the CTR measurement for the NUV-HD of 119 ps was almost identical to that of the Hamamatsu SiPM. It is important to highlight the similar behavior of the CTR, even though the NUV-HD has a better SPTR than the Hamamatsu SiPM. One explanation for this discrepancy may be the increment in device capacitance of the FBK compared to the Hamamatsu sensor. This greater capacitance and thus greater recovery time might cause more pile-up effects, which produce baseline fluctuations in the leading-edge comparator, leading to a deterioration in the time response. Another reason could be the intrinsic parameters of each sensor, PDE is similar in both sensors [16], but cross-talk is worse in the FBK SiPM and also cause a deterioration in the CTR [66], [67].

The HPK SiPM S13360-3050CS (3×3 mm^2 pixel, 50 µm cell) and the LSO:Ce 0.4% Ca crystal measuring $2 \times 2 \times 5$ mm^3 were selected to compare performance with the NINO. A comparison of CTR between the two electronics for a range of over-voltages between 3 V and 10 V is shown in Fig. 24. The NINO ASIC obtained a ≈15% better CTR with respect to the HRFlexToT. One explanation for this discrepancy may be the use of a differential input for the SiPM readout instead of a single-ended anode readout for the HRFlexToT.

Fig. 25 shows that CTR values increased from 117 ps to 175 ps at FWHM for a crystal measuring 20 mm long. This effect is mainly caused by an increase in the light transit time spread and the gamma interaction point fluctuation related to

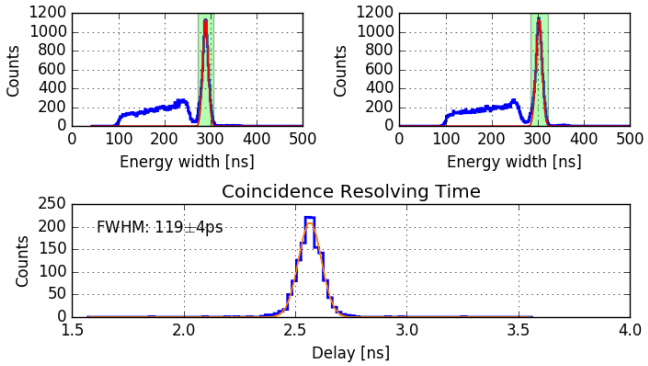

Fig. 23. CTR measurement with LSO:Ce Ca 0.4% measuring 2 × 2 × 5 mm^3 coupled to a NUV-HD SiPM (4 × 4 mm^2 pixel, 40 µm cell) at 9 V of over-voltage.

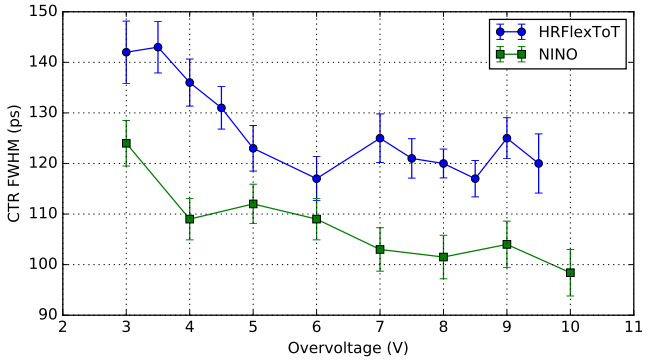

Fig. 24. CTR comparison between the new HRFlexToT and the NINO ASIC from CERN. Sensor used: HPK SiPM S13360-3050CS (3 × 3 mm^2 pixel, 50 µm cell). Crystal used: 2 × 2 × 5 mm^3 LSO:Ce 0.4% Ca.

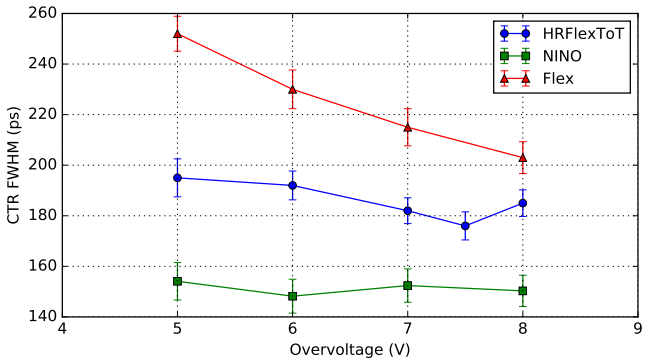

Fig. 25. CTR comparison between the new HRFlexToT, the FlexToT and NINO ASIC from CERN. Sensor used: Hamamatsu SiPM S13360-3075CS (3 × 3 mm^2 pixel, 75 µm cell). Crystal used: 3 × 3 × 20 mm^3 LYSO:Ce.

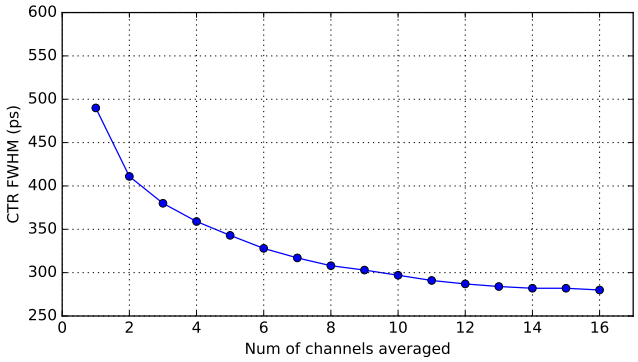

Fig. 26. CTR measurements using a monolithic LFS crystal measuring 25 × 25 × 20 mm^3 coupled to a S13361-6050NE-04 with 6 × 6 mm^2 pixel size, as a function of the number of channels averaged. A 2 × 2 × 5 mm^3 LSO:Ce Ca 0.4% coupled to a S13360-3050CS was utilized as reference detector.

the depth-of-interaction (DOI) of the crystal [68].

Fig. 25 shows a comparison of the CTR obtained with long LYSO:Ce crystals measuring 3 × 3 × 20 mm^3, using the NINO, HRFlexToT, and FlexToT ASICs. The HRFlexToT shows a ≈ 15% improvement in CTR with respect to the previous FlexToT ASIC, thus representing a large improvement in the electronic jitter contribution. Lastly, NINO similarly presents a ≈ 15% improvement in CTR compared to the HRFlexToT when using smaller crystals.

E. CTR measurements with monolithic scintillators

The HRFlexToT was evaluated with a monolithic LFS crystal measuring 25 × 25 × 20 mm^3, wrapped in 3 layers of Teflon and coupled to a 16-channel SiPM array (S13361-6050NE-04, 6 × 6 mm^2 pixel size, 50 µm cell). As depicted in Fig. 26, a CTR of 280 ps was obtained after applying time-walk and time-skew calibration. A second correction was applied by averaging the timestamp of the N fastest channels, and the best results were obtained when considering all channels. Therefore, the expected time resolution for two identical modules using this large monolithic crystal would be around 324 ps FWHM after subtracting the jitter from the reference detector and the TDCs.

The energy resolution at 511 keV of a large monolithic crystal was also studied. All the walls of a 25 × 25 × 10 mm^3 LYSO:Ce crystal were painted black and a Retro Reflector (RR) layer was placed on the top surface. The energy resolution is given in % of FWHM for different beam impact positions, as depicted in Table III. The best values were obtained near the center of the crystal, whereas the edges presented a degradation in the energy resolution because of the poorer light collection efficiency (many of the optical photons generated were lost on the black walls).

V. Discussion

The new, redesigned HRFlexToT presents a lower power consumption, reduced from 11 mW/ch to 3.5 mW/ch, and better time and energy performance compared to its predecessor. The HRFlexToT also presents a larger dynamic range thanks to its linear behavior at low energies, which was the main limitation for some applications of the FlexToT ASIC [37]. Moreover, it enables the readout of pixelated and monolithic scintillator crystals by providing the time and energy measurement for each individual channel.

The ASIC shows promising performances that are the same or better compared to other electronics. To the best of the

TABLE III
ENERGY RESOLUTION AT 511 KEV EXPRESSED IN % OF FWHM. BLUE BOXES INDICATE BEAM IMPACTS CLOSE TO THE EDGES OF THE CRYSTAL. YELLOW BOXES REPRESENT BEAM IMPACTS CLOSE TO THE CENTER OF THE CRYSTAL.

21.9	15.1	14.8	18.2	18.7
16.0	15.5	13.9	14.0	13.7
16.4	13.8	14.2	14.9	14.8
18.9	18.9	14.2	17.8	14.7

authors' knowledge, the HRFlexToT yields the best time resolution in terms of SPTR (142 ps FWHM) for a FBK SiPM NUV-HD (4×4 mm^2 pixel, 40 μm cell) compared to other ASICs reported in the literature where both time and energy measurements are given. Although the NINO ASIC has a better SPTR (7 ps of improvement), an additional circuitry is required to provide a linear energy measurement [68].

Experimental results showed a CTR of 117 ps and 119 ps FWHM for crystals (LSO:Ce, Ca 0.4%) coupled to a Hamamatsu SiPM S13360-3050CS and a FBK SiPM NUV-HD (4×4 mm^2 pixel, $40\,\mu$m cell), respectively. The NINO ASIC still achieves a CTR of 97 ps for the same setup, but with nearly 8 times more power consumption and without a linear energy measurement to capture the 511 keV photopeak. The lower CTR achieved by NINO might be obtained thanks to the use of a differential input readout, whereas the HRFlexToT is connected to the SiPM via a single-ended anode connection.

A comparison between the HRFlexToT and other ASICs in the literature is shown in Table IV. For instance, TOFPET2 or PETIROC2A achieve slightly worse performance than the HRFlexToT, but include internal TDCs for digitization of timestamps. Other ASICs, such as TRIROC, PETA, or STIC3, also employ an internal TDC for their measurements, but SPTR data are not available in the literature for comparison (except for STIC3, but this employs a rather small SiPM). The SPTR achieved by the HRFlexToT is only $\approx$16% worse than the one obtained by the HF readout for the Hamamatsu SiPM S13360-3050CS, with the advantage of much lower power consumption.

One important aspect to consider is the use or not of an internal TDC inside the Front-End ASIC. The advantages of having an internal TDC are: 1) It is only necessary to manufacture one ASIC, thus reducing manufacturing costs; 2) from a system point of view, the PET module only requires one ASIC to capture events and a simple FPGA to process the data and send them to the acquisition system (computer). On the other hand, the benefits of having a TDC external to the ASIC are: 1) renders the system more versatile since any TDC can be employed, either an ASIC or an FPGA-based TDC; 2) It eliminates noise induced by the digital circuitry of the TDC, which affects the time measurement, i.e., the clock-induced noise; 3) the Front-End ASIC must be placed as close as possible to the sensor to optimize its time response and thus power consumption near the SiPM is lower if the TDC is implemented in another chip. Hence, the option selected will depend on the system requirements.

The use of a TDC implemented in an ASIC or an FPGA is also a design decision. Current IC technologies enable use of TDCs in ASICs with a few ps' time resolution, as previously detailed in section I. For instance, the MATRIX ASIC has a sigma time bin resolution of around 10 ps. Current low cost FPGAs enable the design of TDCs with good resolution, such as the Altera Cyclone III, here employed with 94 ps FWHM time bin resolution (40 ps sigma). The selection of one option over another will also depend on the design requirements in terms of power, cost, and time resolution. Usually, TDC ASICs can be designed with lower power consumption than FPGA-based TDCs since the FPGA contains more circuitry. In terms of time resolution, a TDC ASIC may show better performance for current technology nodes with a similar power budget, since the electronics are optimized for that application. Lastly, the development and manufacturing costs of an ASIC are more expensive than for common FPGAs.

Here, we employed both an oscilloscope and an FPGA-based TDC for characterization of the ASIC. However, the HRFlexToT ASIC can also be directly connected to the MATRIX ASIC [19], a 4-channel TDC chip with 10-ps time resolution and 11 mW/ch of power consumption, to digitize the Fast Timing OR output response provided by the HRFlexToT. Recently, this group has developed a new version of the MATRIX ASIC, including 16 channels with the same time resolution (10 ps), lower power consumption ($\approx$ 8.2 mW/ch), and also capable of processing the time+energy output. The combination of the HRFlexTOT and the MATRIX ASICs will form a complete readout system providing digitized data for TOF-PET image reconstruction.

VI. CONCLUSIONS

The HRFlexToT ASIC is a new version of the FlexToT ASIC that incorporates new features, presents a better performance, and is also suitable for TOF-PET applications. A complete evaluation has been conducted of the HRFlexToT ASIC employing either pixelated or monolithic scintillators. The HRFlexToT presents a large dynamic range and an excellent time resolution with low power consumption (3.5 mW/ch). Experimental measurements showed an SPTR of 142 ps and 167 ps FWHM utilizing an FBK SiPM NUV-HD (4×4 mm^2 pixel, $40\,\mu$m cell) and a Hamamatsu SiPM S13360-3050CS, respectively. A CTR of 117 ps and 119 ps FWHM was achieved for the same HPK and FBK SiPMs coupled to LSO:Ce, Ca 0.4% crystals. A module with two large cross-section, Teflon wrapped monolithic crystals (LFS crystal measuring $25 \times 25 \times 20$ mm^3) coupled to an SiPM array (S13361-6050NE-04, 6×6 mm^2, $50\,\mu$m pixel pitch) achieved a CTR of 324 ps FWHM after time-walk and time-skew calibration with the HRFlexToT ASIC.

Experimental measurements comparing HRFlexToT and NINO performance have demonstrated the potential capabilities of the ASIC for fast timing applications. Future work will

TABLE IV
PERFORMANCE COMPARISON BETWEEN DIFFERENT ASICS SUITABLE FOR TOF-PET APPLICATIONS. THE HF READOUT IS ALSO SHOWN TO ILLUSTRATE THE TIME RESOLUTION THAT CAN BE ACHIEVED WITH AN ALMOST "PERFECT" ELECTRONICS WITH CURRENT SENSORS.

ASIC	Power in mW/ch	SPTR in ps FWHM	SiPM Model	Timestamp Time bin	Reference
HF readout	720	144 92	S13360-3050PE NUV-HD (4×4, 40 µm)	External	[40], [41]
NINO	27	160 135	S13360-3050CS NUV-HD (4×4, 40 µm)	External	[23], [40], This study
HRFlexToT	3.5	167 142	S13360-3050CS NUV-HD (4×4, 40 µm)	External	This study
FlexToT	11	214	S13360-3050CS	External	[25]
PETIROC2A	6	190	S13360-3050PE	30 ps	[26]
TRIROC	10	-	-	40 ps	[28]
STIC3	25	150	S13360-1350CS	50 ps	[32], [33]
PETA	40	-	-	50 ps	[36]
TOFPET2	8.2	212	S13361-3050AE-04	30 ps	[29]

include experimental measurements using larger SiPM arrays with several HRFlexToT and MATRIX ASICs. Moreover, the HRFlexToT will be tested with other scintillator crystals capable of capturing prompt light, such as Cherenkov light [41], [69]–[71].

ACKNOWLEDGMENTS

The authors would like to thank S. Gundacker and E. Auffray for collaborating in the experiments comparing the HRFlexToT and the NINO ASIC. These experimental results are based on work during a short-term scientific mission (STSM) at the Conseil Européen pour la Recherche Nucléaire (CERN) Crystal Clear lab in the framework of COST (European Cooperation in Science and Technology) Action TD1401 - Fast advanced Scintillator Timing (FAST) [72].

REFERENCES

[1] J. J. Vaquero and P. Kinahan, "Positron Emission Tomography: Current Challenges and Opportunities for Technological Advances in Clinical and Preclinical Imaging Systems." *Annu Rev Biomed Eng.*, vol. 17, no. 1, pp. 385–414, 2015. [Online]. Available: https://doi.org/10.1146/annurev-bioeng-071114-040723

[2] S. R. Cherry, T. Jones, J. S. Karp, J. Qi, W. W. Moses, and R. D. Badawi, "Total-Body PET: Maximizing Sensitivity to Create New Opportunities for Clinical Research and Patient Care." *J Nucl Med.*, pp. 3–12, 2018. [Online]. Available: https://doi.org/doi:10.2967/jnumed.116.184028

[3] S. Surti, A. R. Pantel, and J. S. Karp, "Total Body PET: Why, How, What for?" *IEEE Transactions on Radiation and Plasma Medical Sciences*, vol. 4, no. 3, 2020. [Online]. Available: https://ieeexplore.ieee.org/stamp/stamp.jsp?arnumber=9056798

[4] M. Carminati and C. Fiorini, "Challenges for Microelectronics in Non-Invasive Medical Diagnostics," *Sensors*, vol. 20, no. 13, p. 3636, jun 2020. [Online]. Available: https://www.mdpi.com/1424-8220/20/13/3636

[5] T. F. Budinger, "Time-of-Flight Positron Emission Tomography: Status Relative to Conventional PET," *Journal of Nuclear Medicine*, vol. 24, no. 1, 1983. [Online]. Available: https://pubmed.ncbi.nlm.nih.gov/6336778/

[6] S. Vandenberghe, E. Mikhaylova, E. D'Hoe, P. Mollet, and J. S. Karp, "Recent developments in time-of-flight PET," *EJNMMI Physics*, vol. 3, no. 1, p. 3, dec 2016. [Online]. Available: https://www.ncbi.nlm.nih.gov/pmc/articles/PMC4754240/

[7] P. Lecoq, "Pushing the Limits in Time-of-Flight PET Imaging," *IEEE Transactions on Radiation and Plasma Medical Sciences*, vol. 1, no. 6, pp. 473–485, nov 2017. [Online]. Available: http://ieeexplore.ieee.org/document/8049484/

[8] S. Gundacker, F. Acerbi, E. Auffray, A. Ferri, A. Gola, M. V. Nemallapudi, G. Paternoster, C. Piemonte, and P. Lecoq, "State of the art timing in TOF-PET detectors with LuAG, GAGG and L(Y)SO scintillators of various sizes coupled to FBK-SiPMs," *Journal of Instrumentation*, vol. 11, 2016. [Online]. Available: https://doi.org/10.1088/1748-0221/11/08/P08008

[9] M. Pizzichemi, A. Polesel, G. Stringhini, S. Gundacker, P. Lecoq, S. Tavernier, M. Paganoni, and E. Auffray, "On light sharing TOF-PET modules with depth of interaction and 157 ps FWHM coincidence time resolution," *Physics in Medicine and Biology*, vol. 64, no. 15, p. 155008, aug 2019. [Online]. Available: https://doi.org/10.1088/1361-6560/ab2cb0

[10] E. Lamprou, A. Gonzalez, F. J. Sanchez, and J. M. Benlloch, "Exploring TOF capabilities of PET detector blocks based on large monolithic crystals and analog SiPMs," *ELSEVIER Physica Medica*, vol. 70, pp. 10–18, 2020. [Online]. Available: https://doi.org/10.1016/j.ejmp.2019.12.004

[11] X. Zhang, X. Wang, N. Ren, B. Hu, B. Ding, Z. Kuang, S. Wu, Z. Sang, Z. Hu, J. Du, D. Liang, X. Liu, H. Zheng, and Y. Yang, "Performance of long rectangular semi-monolithic scintillator PET detectors," *Medical Physics*, vol. 46, no. 4, pp. 1608–1619, apr 2019. [Online]. Available: https://pubmed.ncbi.nlm.nih.gov/30723932/

[12] G. Konstantinou, R. Chil, M. Desco, and J. J. Vaquero, "Subsurface Laser Engraving Techniques for Scintillator Crystals: Methods, Applications, and Advantages," *IEEE Transactions on Radiation and Plasma Medical Sciences*, vol. 1, no. 5, pp. 377–384, jun 2017. [Online]. Available: https://doi.org/10.1109/trpms.2017.2714265

[13] S. Gomez, D. Gascon, G. Fernández, A. Sanuy, J. Mauricio, R. Graciani, and D. Sanchez, "MUSIC: An 8 channel readout ASIC for SiPM arrays," *Proc. SPIE 9899, Optical Sensing and Detection IV*, vol. 9899, 2016. [Online]. Available: https://doi.org/10.1117/12.2231095

[14] S. Gundacker and A. Heering, "The silicon photomultiplier: Fundamentals and applications of a modern solid-state photon detector," pp. 17–18, sep 2020. [Online]. Available: https://doi.org/10.1088/1361-6560/ab7b2d

[15] S. Seifert, H. T. Van Dam, R. Vinke, P. Dendooven, H. Löhner, F. J. Beekman, and D. R. Schaart, "A comprehensive model to predict the timing resolution of SiPM-based scintillation detectors: Theory and experimental validation," *IEEE Transactions on Nuclear Science*, vol. 59, no. 1 PART 2, pp. 190–204, feb 2012. [Online]. Available: https://doi.org/10.1109/TNS.2011.2179314

[16] F. Acerbi and S. Gundacker, "Understanding and simulating SiPMs," *Nuclear Instruments and Methods in Physics Research Section A: Accelerators, Spectrometers, Detectors and Associated Equipment*, vol. 926, pp. 16–35, 2019. [Online]. Available: https://doi.org/10.1016/j.nima.2018.11.118

[17] Hamamatsu Photonics K.K., "Si APD, MPPC." [Online]. Available: https://www.hamamatsu.com/resources/pdf/ssd/e03_handbook_si_apd_mppc.pdf

[18] J. Mazorra, H. Chanal, A. Comerma, D. Gascón, S. Gómez, X. Han, N. Pillet, and R. Vandaele, "PACIFIC: the readout ASIC for the SciFi Tracker of the upgraded LHCb detector," *Journal of Instrumentation*, vol. 11, no. 02, pp. C02 021–C02 021, feb 2016.

[Online]. Available: http://stacks.iop.org/1748-0221/11/i=02/a=C02021?key=crossref.76341f2dc0505f8f2ae7f25a2d1bf853

[19] J. Mauricio, D. Gascón, D. Ciaglia, S. Gómez, G. Fernández, and A. Sanuy, "MATRIX: A 15 ps resistive interpolation TDC ASIC based on a novel regular structure," in *Journal of Instrumentation*, vol. 11, no. 12, 2016. [Online]. Available: https://doi.org/10.1088/1748-0221/11/12/C12047

[20] J. Van Sluis, "Performance characteristics of the digital Biograph Vision PET/CT system," pp. 1031–1036, jul 2019. [Online]. Available: https://pubmed.ncbi.nlm.nih.gov/30630944/

[21] V. Nadig, B. Weissler, H. Radermacher, V. Schulz, and D. Schug, "Investigation of the Power Consumption of the PETsys TOFPET2 ASIC," *IEEE Transactions on Radiation and Plasma Medical Sciences*, vol. 4, pp. 378–388, 2020. [Online]. Available: https://doi.org/10.1109/TRPMS.2019.2955032

[22] D. Schug, V. Nadig, B. Weissler, P. Gebhardt, and V. Schulz, "Initial measurements with the PETsys TOFPET2 ASIC evaluation kit and a characterization of the ASIC TDC," aug 2018. [Online]. Available: https://ieeexplore.ieee.org/document/8556088

[23] F. Anghinolfi, P. Jarron, A. N. Martemiyanov, E. Usenko, H. Wenninger, M. C. S. Williams, and A. Zichichid, "NINO: an ultra-fast and low-power front-end amplifier/discriminator ASIC designed for the multigap resistive plate chamber," *Nuclear Instruments and Methods in Physics Research Section A: Accelerators, Spectrometers, Detectors and Associated Equipment*, vol. 533, 2004. [Online]. Available: https://doi.org/10.1016/j.nima.2004.07.024

[24] S. Gundacker, E. Auffray, B. Frisch, P. Jarron, A. Knapitsch, T. Meyer, M. Pizzichemi, and P. Lecoq, "Time of flight positron emission tomography towards 100ps resolution with L(Y)SO: An experimental and theoretical analysis," *Journal of Instrumentation*, vol. 8, no. 7, jul 2013. [Online]. Available: https://doi.org/10.1088/1748-0221/8/07/P07014

[25] I. Sarasola, M. V. Nemallapudi, S. Gundacker, D. Sánchez, D. Gascón, P. Rato, J. Marín, and E. Auffray, "A comparative study of the time performance between NINO and FlexToT ASICs," *Journal of Instrumentation*, vol. 12, no. 4, p. P04016, apr 2017. [Online]. Available: https://doi.org/10.1088/1748-0221/12/04/P04016

[26] S. Ahmad, J. Fleury, J. B. Cizel, C. De La Taille, N. Seguin-Moreau, S. Gundacker, and E. Auffray-Hillemanns, "Petiroc2A: Characterization and Experimental Results," in *2018 IEEE Nuclear Science Symposium and Medical Imaging Conference, NSS/MIC 2018 - Proceedings*. Institute of Electrical and Electronics Engineers Inc., nov 2018. [Online]. Available: https://doi.org/10.1109/NSSMIC.2018.8824464

[27] "Weeroc." [Online]. Available: https://www.weeroc.com/products/see-catalogue

[28] S. Ahmad, C. De La Taille, J. Fleury, N. Seguin-Moreau, L. Raux, S. Callier, G. Martin-Chassard, F. Dulucq, and D. Thienpont, "Triroc, a versatile 64-channel SiPM readout ASIC for time-of-flight PET," in *2016 IEEE Nuclear Science Symposium, Medical Imaging Conference and Room-Temperature Semiconductor Detector Workshop, NSS/MIC/RTSD 2016*, vol. 2017-Janua. TRIROC: Institute of Electrical and Electronics Engineers Inc., oct 2017. [Online]. Available: https://doi.org/10.1109/NSSMIC.2016.8069882

[29] R. Bugalho, A. Di Francesco, L. Ferramacho, C. Leong, T. Niknejad, L. Oliveira, M. Rolo, J. C. Silva, R. Silva, M. Silveira, S. Tavernier, and J. Varela, "Experimental characterization of the TOFPET2 ASIC," *IOP Publishing*, vol. 14, no. 3, 2019. [Online]. Available: https://doi.org/10.1088/1748-0221/14/03/p03029

[30] E. Lamprou, A. González-Montoro, G. Cañizares, V. Ilisie, J. Barrio, F. Sánchez, A. J. González, and J. M. Benlloch, "Characterization of TOF-PET detectors based on monolithic blocks and ASIC-readout," jun 2018. [Online]. Available: http://arxiv.org/abs/1806.08715

[31] "PETsys Electronics." [Online]. Available: https://www.petsyselectronics.com/web/

[32] Y. Munwes, K. Briggl, H. Chen, T. Harion, H. C. Schultz-Coulon, W. Shen, and V. Stankova, "Single photon time resolution with silicon photomultipliers using the STiC readout chip," in *2015 IEEE Nuclear Science Symposium and Medical Imaging Conference, NSS/MIC 2015*. Institute of Electrical and Electronics Engineers Inc., oct 2016. [Online]. Available: https://doi.org/10.1109/NSSMIC.2015.7581738

[33] H. Chen, K. Briggl, P. Fischer, A. Gil, T. Harion, Y. Munwes, M. Ritzert, D. Schimansky, H. C. Schultz-Coulon, W. Shen, and V. Stankova, "A dedicated readout ASIC for Time-of-Flight Positron Emission Tomography using Silicon Photomultiplier (SiPM)," in *2014 IEEE Nuclear Science Symposium and Medical Imaging Conference, NSS/MIC 2014*. Institute of Electrical and Electronics Engineers Inc., mar 2016. [Online]. Available: https://doi.org/10.1109/NSSMIC.2014.7431045

[34] H. Chen, K. Briggl, P. Eckert, T. Harion, Y. Munwes, W. Shen, V. Stankova, and H. C. Schultz-Coulon, "MuTRiG: A mixed signal Silicon Photomultiplier readout ASIC with high timing resolution and gigabit data link," in *Journal of Instrumentation*, vol. 12, no. 1. Institute of Physics Publishing, jan 2017, p. C01043. [Online]. Available: https://iopscience-iop-org.sire.ub.edu/article/10.1088/1748-0221/12/01/C01043https://iopscience-iop-org.sire.ub.edu/article/10.1088/1748-0221/12/01/C01043/meta

[35] M. Ahnen, R. Becker, A. Buck, C. Casella, V. Commichau, D. di Calafiori, G. Dissertori, A. Eleftheriou, J. Fischer, A. S. Howard, M. Ito, P. Khateri, J. Kim, W. Lustermann, C. Ritzer, U. Roser, M. Rudin, P. Solevi, C. Tsoumpas, G. Warnock, B. Weber, M. Wyss, and A. Zagozdzinska-Bochenek, "Performance Measurements of the SAFIR Prototype Detector With the STiC ASIC Readout," *IEEE Transactions on Radiation and Plasma Medical Sciences*, vol. 2, no. 3, pp. 250–258, jan 2018. [Online]. Available: https://doi.org/10.1109/trpms.2018.2797484

[36] I. Sacco, P. Fischer, and M. Ritzert, "PETA4: A multi-channel TDC/ADC ASIC for SiPM readout," *Journal of Instrumentation*, vol. 8, no. 12, pp. 23–27, 2013. [Online]. Available: https://doi.org/10.1088/1748-0221/8/12/C12013

[37] A. Comerma, D. Gascon, L. Freixas, L. Garrido, R. Graciani, J. Marin, G. Martinez, J. M. Perez, P. R. Mendes, J. Castilla, J. M. Cela, J. M. Fernandez-Varea, and I. Sarasola, "FlexToT - Current mode ASIC for readout of common cathode SiPM arrays," in *IEEE Nuclear Science Symposium Conference Record*. Institute of Electrical and Electronics Engineers Inc., 2013. [Online]. Available: https://doi.org/10.1109/NSSMIC.2013.6829761

[38] J. Trenado, J. M. Cela, A. Comerma, D. Gascon, R. Graciani, L. Freixas, J. Marin, G. Martínez, R. Masachs, J. M. Perez, P. Rato, D. Sanchez, A. Sanuy, and I. Sarasola, "Performance of FlexToT time based PET readout ASIC for depth of interaction measurements," in *Proceedings of Science*, vol. 213. Proceedings of Science (PoS), jul 2014, p. 241. [Online]. Available: https://pos.sissa.it/213/241

[39] J. M. Cela, L. Freixas, J. I. Lagares, J. Marin, G. Martinez, J. Navarrete, J. C. Oller, J. M. Perez, P. Rato-Mendes, I. Sarasola, O. Vela, J. M. Fernandez-Varea, D. Gascon, S. Gomez, R. Graciani, J. Mauricio, D. Sanchez, A. Sanuy, O. de la Torre, and D. Badia, "A Compact Detector Module Design Based on FlexToT ASICs for Time-of-Flight PET-MR," *IEEE Transactions on Radiation and Plasma Medical Sciences*, vol. 2, no. 6, pp. 549–553, sep 2018. [Online]. Available: https://doi.org/10.1109/trpms.2018.2870927

[40] S. Gundacker, R. M. Turtos, E. Auffray, M. Paganoni, and P. Lecoq, "High-frequency SiPM readout advances measured coincidence time resolution limits in TOF-PET," *Physics in Medicine and Biology*, vol. 64, no. 5, pp. 55 012–55 021, feb 2019. [Online]. Available: https://doi.org/10.1088/1361-6560/aafd52

[41] S. Gundacker, R. Martinez Turtos, N. Kratochwil, R. H. Pots, M. Paganoni, P. Lecoq, and E. Auffray, "Experimental time resolution limits of modern SiPMs and TOF-PET detectors exploring different scintillators and Cherenkov emission," *Physics in Medicine and Biology*, vol. 65, no. 2, p. 25001, jan 2020. [Online]. Available: https://doi.org/10.1088/1361-6560/ab63b4

[42] Infineon, "BGA616 Silicon Germanium Broadband MMIC Amplifier RF and Protection Devices," 2011. [Online]. Available: https://www.infineon.com/dgdl/Infineon-BGA616-DS-v02_01-en.pdf?fileId=db3a304314dca3890115419102bb163b

[43] L. Perktold and J. Christiansen, "A multichannel time-to-digital converter ASIC with better than 3ps RMS time resolution," *Journal of Instrumentation*, vol. 9, no. 1, p. C01060, jan 2014. [Online]. Available: https://doi.org/10.1088/1748-0221/9/01/C01060

[44] F. Dadouche, T. Turko, W. Uhring, I. Malass, J. Bartringer, and J.-p. L. Normand, "Design Methodology of TDC on Low Cost FPGA Targets Case Study : Implementation of a 42 ps Resolution TDC on a Cyclone IV FPGA Target ." in *Conference: SENSORCOMM 2015*, no. c, 2015, pp. 29–34. [Online]. Available: https://www.researchgate.net/publication/283355485_Design_Methodology_of_TDC_on_Low_Cost_FPGA_Targets_Case_Study_Implementation_of_a_42_ps_Resolution_TDC_on_a_Cyclone_IV_FPGA_Target

[45] Y. Zhang, Min and Wang, Hai and Liu, "A 7.4 ps FPGA-Based TDC with a 1024-Unit Measurement Matrix," *Sensors*, vol. 17, no. 4, 2017. [Online]. Available: https://doi.org/10.3390/s17040865

[46] P. Carra, M. Bertazzoni, M. G. Bisogni, J. M. Cela Ruiz, A. Del Guerra, D. Gascon, S. Gomez, M. Morrocchi, G. Pazzi, D. Sanchez, I. Sarasola Martin, G. Sportelli, and N. Belcari, "Auto-Calibrating TDC for an SoC-FPGA Data Acquisition System," *IEEE Transactions on Radiation*

and Plasma Medical Sciences, vol. 3, no. 5, pp. 549–556, nov 2018. [Online]. Available: https://doi.org/10.1109/trpms.2018.2882709

[47] S. Gómez, A. Sanmukh, D. Gascón, D. Sánchez, J. Mauricio, R. Graciani, R. Manera, L. Garrido, J. M. Fernández-Varea, J. M. Cela, L. Freixas, J. Marín, J. J. Navarrete, J. C. Oller, J. M. Pérez, P. Rato Mendes, and O. Vela, "A High Dynamic Range ASIC for Time of Flight PET with monolithic crystals," in *Proceedings of Science*, vol. 343. Sissa Medialab Srl, jul 2018, pp. 17–21. [Online]. Available: https://pos.sissa.it/343/085/

[48] S. Gomez, D. Sanchez, D. Gascon, J. M. Cela, L. Freixas, R. Graciani, R. Manera, J. Marin, J. Mauricio, J. J. Navarrete, J. C. Oller, J. M. Perez, P. Rato Mendes, A. Sanmukh, and O. Vela, "A High Dynamic Range ASIC for Time of Flight PET with pixelated and monolithic crystals," in *2019 IEEE Nuclear Science Symposium and Medical Imaging Conference, NSS/MIC 2019*. Institute of Electrical and Electronics Engineers Inc., oct 2019. [Online]. Available: https://doi.org/10.1109/NSS/MIC42101.2019.9059762

[49] D. Gascon, A. Comerma, and L. Freixas, "Readout circuits for multi-channel photomultiplier arrays, European Patent: EP 12382516.8," 2012. [Online]. Available: https://worldwide.espacenet.com/patent/search/family/047713793/publication/EP2936207B1?q=pn%3DEP2936207B1%3F

[50] F. Yuan, "Low-voltage CMOS current-mode circuits: topology and characteristics," *IEE Proceedings - Circuits, Devices and Systems*, vol. 153, no. 3, pp. 219–230(11), 2006. [Online]. Available: http://digital-library.theiet.org/content/journals/10.1049/ip-cds_20045058

[51] J. Ramirez-Angulo, R. G. Carvajal, and A. Torralba, "Low Supply Voltage High-Performance CMOS Current Mirror With Low Input and Output Voltage Requirements," *IEEE Transactions on Circuits and Systems II: Express Briefs*, vol. 51, no. 3, pp. 124–129, mar 2004. [Online]. Available: https://www.researchgate.net/publication/3452011_Low_Supply_Voltage_High-Performance_CMOS_Current_Mirror_With_Low_Input_and_Output_Voltage_Requirements

[52] S. M. Park and C. Toumazou, "Low noise current-mode CMOS transimpedance amplifier for giga-bit optical communication," in *ISCAS '98. Proceedings of the 1998 IEEE International Symposium on Circuits and Systems (Cat. No.98CH36187)*, vol. 1. IEEE, 1998, pp. 293–296. [Online]. Available: http://ieeexplore.ieee.org/articleDetails.jsp?arnumber=704419

[53] R. del Rio-Fernandez, G. Linan-Cembrano, R. Dominguez-Castro, and A. Rodriquez-Vazquez, "Mismatch-insensitive high-accuracy high-speed continuous-time current comparator in low voltage CMOS," in *IEEE-CAS Region 8 Workshop on Analog and Mixed IC Design, Proceedings*. IEEE, 1997, pp. 111–116. [Online]. Available: https://doi.org/10.1109/amicd.1997.637202

[54] V. V. Ivanov and I. M. Filanovsky, *Operational Amplifier Speed and Accuracy Improvement*, 1st ed. Springer US, 2004, vol. 763. [Online]. Available: https://doi.org/10.1007/b105872

[55] G. De Geronimo, P. O'Connor, and A. Kandasamy, "Analog CMOS peak detect and hold circuits. Part 1. Analysis of the classical configuration," *Nuclear Instruments and Methods in Physics Research Section A: Accelerators, Spectrometers, Detectors and Associated Equipment*, vol. 484, no. 1, pp. 533–543, 2002. [Online]. Available: https://doi.org/10.1016/S0168-9002(01)02059-9

[56] ——, "Analog CMOS peak detect and hold circuits. Part 2. The two-phase offset-free and derandomizing configuration," *Nuclear Instruments and Methods in Physics Research, Section A: Accelerators, Spectrometers, Detectors and Associated Equipment*, vol. 484, no. 1-3, pp. 544–556, may 2002. [Online]. Available: https://www.sciencedirect.com/science/article/pii/S0168900201020605

[57] W. M. C. Sansen, *Analog Design Essentials*, 1st ed. Springer US, 2006, vol. 859. [Online]. Available: https://doi.org/10.1007/b135984

[58] P. E. Allen and D. R. Holberg, *CMOS Analog Circuit Design*. Oxford University Press, 2002.

[59] "Electronics Instrumentation Service from Uniersity of Barcelona (SIUB)." [Online]. Available: http://siub.ub.edu/downloads/hrflextot/

[60] M. V. Nemallapudi, S. Gundacker, P. Lecoq, and E. Auffray, "Single photon time resolution of state of the art SiPMs," *Journal of Instrumentation*, vol. 11, no. 10, oct 2016. [Online]. Available: https://doi.org/10.1088/1748-0221/11/10/P10016

[61] R. D. Badawy, "First human imaging studies with the EXPLORER total-body PET scanner," pp. 299–303, jul 2019. [Online]. Available: https://pubmed.ncbi.nlm.nih.gov/30733314/

[62] Hamamatsu Photonics K.K., "Physics and operation of the MPPC silicon photomultiplier." [Online]. Available: https://hub.hamamatsu.com/jp/en/technical-note/sipm-physics-operation/index.html

[63] D. Renker and E. Lorenz, "Advances in solid state photon detectors," *Journal of Instrumentation*, vol. 4, no. 04, pp. P04 004———P04 004, 2009. [Online]. Available: http://stacks.iop.org/1748-0221/4/i=04/a=P04004?key=crossref.0b2aaff32d46c072c53ee73cbf621d59

[64] G. Collazuol, "The SiPM physics and technology-a review," in *International Workshop on New Photon-Detectors (PhotoDet 2012)*, 2012. [Online]. Available: https://indico.cern.ch/event/164917/contributions/1417121/attachments/198512/278663/PhotoDet12_-_collazuol_-_v3.pdf

[65] Hamamatsu Photonics K.K., "S13360 series - MPPCs for precision measurement." [Online]. Available: https://www.hamamatsu.com/resources/pdf/ssd/s13360_series_kapd1052e.pdf

[66] A. Gola, F. Acerbi, M. Capasso, M. Marcante, A. Mazzi, G. Paternoster, C. Piemonte, V. Regazzoni, and N. Zorzi, "NUV-sensitive silicon photomultiplier technologies developed at fondazione Bruno Kessler," *Sensors (Switzerland)*, vol. 19, no. 2, p. 308, jan 2019. [Online]. Available: http://www.mdpi.com/1424-8220/19/2/308

[67] Hamamatsu Photonics K.K., "MPPCs for precision measurement: S13360 series." [Online]. Available: https://www.hamamatsu.com/resources/pdf/ssd/s13360_series_kapd1052e.pdf

[68] S. Gundacker, A. Knapitsch, E. Auffray, P. Jarron, T. Meyer, and P. Lecoq, "Time resolution deterioration with increasing crystal length in a TOF-PET system," *Nuclear Instruments and Methods in Physics Research, Section A: Accelerators, Spectrometers, Detectors and Associated Equipment*, vol. 737, pp. 92–100, feb 2014. [Online]. Available: https://doi.org/10.1016/j.nima.2013.11.025

[69] N. Kratochwil, E. Auffray, and S. Gundacker, "Exploring Cherenkov emission of BGO for TOF-PET," *IEEE Transactions on Radiation and Plasma Medical Sciences*, pp. 1–1, oct 2020. [Online]. Available: https://doi.org/10.1109/trpms.2020.3030483

[70] G. Ariño-Estrada, G. S. Mitchell, and H. et al Kim, "First Cerenkov Charge-Induction (CCI) TlBr Detector for TOF-PET and Proton Range Verification," *Phys Med Biol.*, vol. 64, no. 17, 2019. [Online]. Available: https://doi.org/10.1088/1361-6560/ab35c4

[71] G. Arino-Estrada, E. Roncali, A. R. Selfridge, J. Du, J. Glodo, K. S. Shah, and S. R. Cherry, "Study of Čerenkov Light Emission in the Semiconductors TlBr and TlCl for TOF-PET," *IEEE Transactions on Radiation and Plasma Medical Sciences*, pp. 1–1, sep 2020. [Online]. Available: https://doi.org/10.1109/trpms.2020.3024032

[72] "Action TD1401 - COST." [Online]. Available: https://www.cost.eu/actions/TD1401/#tabs%7CName:overview